Offshore Tsunami Deposits: Evidence from Sediment Cores and Numerical Wave Propagation of the 1601 CE Lake Lucerne Event

Valentin Nigg[1], Paola Bacigaluppi[2], David F. Vetsch[2], Hendrik Vogel[1], Katrina Kremer[1, 3], and Flavio S. Anselmetti[1]

[1]Institute of Geological Sciences and Oeschger Centre for Climate Change Research, University of Bern, Bern, Switzerland, [2]Laboratory of Hydraulics, Hydrology and Glaciology, ETH Zurich, Zurich, Switzerland, [3]Swiss Seismological Service, ETH Zurich, Zurich, Switzerland

Corresponding author: Valentin Nigg (valentin.nigg@geo.unibe.ch)

Key Points:

- A siliciclastic-rich, normally graded sediment deposit is associated with the 1601 CE Lake Lucerne tsunami event
- Sedimentological analysis and radiocarbon dating were combined with numerical wave propagation to support the proposed depositional model
- Numerical simulation of the dimensionless bed shear-stress indicates area of potential erosion in the offshore environment

Abstract

The 1601 Common Era earthquake (Mw ca. 5.9) in "Unterwalden", Central Switzerland triggered multiple subaqueous mass movements and a subaerial rockfall that generated tsunami waves with devastating run-up heights of up to 4 m and several hundred meters of inundation along the coastal lowland plain of Lake Lucerne. In the shallow Lucerne Bay at the outlet of the perialpine lake, historical chronicles reported a seiche with an initial amplitude of ~1–2 m and a period of 10 min that decreased with time but persisted for several days after the event. The impact and erosion potential of the tsunami wave on the Lucerne Bay is assessed with sediment core analysis and numerical simulation of wave propagation. A 60 cm thick offshore event deposit was recovered and radiocarbon dated along a sediment-core transect. The event deposit has a sharp basal contact with carbonate shell fragments and a normal graded succession of siliciclastic sand to silt with high amount of terrestrial-derived horizontally bedded wooden particles. The simulated tsunami waves have a water-surface displacement of up to 1.5 m and bed shear-stresses that are likely capable of remobilizing large amounts of sediment in the Lucerne Bay area. Our study thus successfully links the sedimentology of event deposits with physical principles of sediment mobilization derived from numerical wave modeling, providing a tool to improve the identification and interpretation of potential tsunami deposits.

Plain Language Summary

An earthquake in Central Switzerland generated a tsunami on Lake Lucerne in the year 1601 that was historically documented. The tsunami waves caused casualities, flooded coastal plains and considerably damaged the lakeshore. Previous studies have shown that several underwater landslides and a rockfall caused by the earthquake generated the tsunami waves that propageated along the several lake basins . To better characterize tsunami hazard in Lake Lucerne, we examined sediment cores from the Lucerne Bay that host a sedimentary deposit, which has been associated to the historically reported evenet in 1601. Additionally, we simulated the tsunami waves with specialized computer codes and studied the erosion potential in the Lucerne Bay.

1 Introduction

Tsunami hazard is frequently associated with megathrust earthquakes at convergent plate boundaries in the marine environment (e.g., 2011 Common Era (CE) Tohoku-Oki tsunami (e.g., Goto et al., 2011a; Suzuki et al., 2011)). But also, earthquake-triggered subaqueous mass movements have generated devastating tsunami inundation in the recent past (e.g., 2018 CE Sulawesi earthquake (e.g., Heiderzadeh et al., 2019)). Moreover, tsunamis in lakes have been recognized as a considerable natural hazard with high magnitudes and low recurrence rates (e.g., Hilbe & Anselmetti, 2015; Kremer et al., 2015; Kremer et al., 2020; Nigg et al., 2021; Strupler et al., 2018a, 2018b). Large subaqueous and subaerial mass movements are considered to be the most common triggering mechanism for the tsunami generation in lakes (e.g., Hilbe & Anselmetti, 2015; Kremer et al., 2020; Mountjoy et al., 2019; Nigg et al., 2021; Roberts et al., 2013; Strupler et al. 2020). Historic chronicles document that lacustrine tsunamis have caused severe shore erosion, inundation, and fatalities (e.g., Cysat, 1969; Hilbe & Anselmetti, 2015; Kremer et al., 2014). For example, lacustrine tsunamis have been reported in historical chronicles at Lake Geneva (564 CE Tauredunum rockfall (Montandon, 1925; Favrod, 1991)), Lake Baikal (1861 CE Tsagan earthquake (Klyuchevskii et al., 2011)), Lake Lucerne (1601 CE Unterwalden earthquake (Cysat, 1969) and 1687 CE Muota Delta collapse (Bünti, 1973; Billeter, 1923; Dietrich, 1689)). Additionally, they have been proposed to occur in the prehistoric period as a consequence of large subaqueous and subaerial mass movements (e.g., Hilbe & Anselmetti, 2014; Kremer et al., 2015; Nigg et al., 2021; Schnellmann et al., 2006; Siegenthaler et al., 1987). And have also been suggested from numerical tsunami simulations (e.g., Hilbe & Anselmetti, 2015; Kremer et al., 2012; Mountjoy et al., 2019) and subaqueous lake morphology (e.g., Gardner et al., 2000; Moore et al., 2006). However, depositional signatures of tsunami impact in the on- and offshore have received little attention in the lacustrine environment. Nevertheless, Roberts et al. (2013) document onshore sedimentary signatures of the 2007 CE subaerial landslide-generated tsunami in Lake Chehalis and Nigg et al. (2021) found sedimentary evidence of a prehistoric tsunami generated by a delta collapse in the shallow water and coastal area of Lake Sils, Switzerland, that are comparable to marine tsunami deposits.

Tsunami deposits are the accumulation of remobilized sediment from tsunami inundation and backwash in the on- and offshore setting (e.g., Einsele et al., 1996), which have been predominantly investigated in marine environments. These deposits have been increasingly studied following the devastating 2004 CE Indian Ocean tsunami (e.g., Feldens et al., 2009; Paris et al., 2010; Sakuna et al., 2012; Sugawara et al., 2009) and 2011 CE Tohoku-Oki tsunami (e.g., Goto et al., 2014; Haraguchi et al., 2013; Ikehara et al., 2014; Yoshikawa et al., 2015; Tamura et al., 2015). Although offshore deposits may contribute to improved tsunami-hazard assessment in the future (Costa et al., 2020), especially in areas with fragmented terrestrial records (Goodman-Tchernov & Austin, 2015), anthropogenically influenced coastal areas (e.g., Fritz et al., 2008; Spiske et al., 2013), limited tsunami preservation (Spiske et al., 2013), and sediment-limited coastal settings (Apotsos et al., 2011), the number of publications examining their signatures is rather small compared to their onshore counterparts (e.g., Dawson and Stewart, 2008; Costa et al., 2020). This may be related to poor preservation of the primary deposits, especially due to reworking by wind-induced bottom currents above the storm-wave base within months (Weiss & Bahlburg, 2006) and by bioturbation from aquatic organisms (van den Bergh et al., 2003). Nevertheless, previous studies have successfully identified historic and prehistoric offshore tsunami deposits in the shallow marine setting (e.g., Abrantes et al., 2008; Goodman-Tchernov et al., 2009; Riou et al., 2020; Smedile et al., 2011; van den Bergh et al., 2003). Their depositional signatures are characterized by a wide range of sedimentological characteristics (e.g., Fujiwara, 2008) including lower erosional surfaces (e.g., Ikehara et al., 2014; Riou et al., 2020; Smedile et al., 2020; Yoshikawa et al., 2015), coarse-grained clastic materials (Abrantes et al., 2008; Goodman-Tchernov et al., 2009; Paris et al., 2010; Sakuna et al., 2012; van den Bergh et al., 2003), terrestrial-derived organics (Goodman-Tchernov et al., 2009; Paris et al., 2010; Sakuna et al., 2012), as well as single- and multiple-graded sandy deposits (e.g., Tamura et al., 2015). Yet, no universal criteria for the recognition offshore tsunami deposits are defined. Nevertheless, multiproxy-based sedimentological and geophysical methods combined with numerical simulation of sediment transport will help to improve the understanding of tsunami-induced sediment remobilization and deposition (e.g., Goto et al., 2011b; Noda et al., 2007).

Tsunami sediment-transport and deposition have increasingly been studied using inverse (e.g., Huntington et al. 2007; Jaffe & Gelfenbaum, 2007; Jaffe et al., 2011; Jaffe et al., 2012; Johnson et al., 2017; Spiske et al., 2010; Tang & Weiss, 2015; Woodruff et al., 2008) and forward modelling (e.g., Apotsos et al., 2011; Apotsos et al., 2012; Ontowirjo et al., 2013; Pritchard & Dickinson, 2008) in the onshore setting to reconstruct tsunami flow speed based on the grain-size distribution of tsunami deposits (Jaffe and Gelfenbaum, 2007). Moreover, forward models combine hydrodynamics and sediment transport models (including erosion and deposition) to simulate observed sedimentary deposits (e.g., grain-size distribution and spatial thickness distribution) (Apotsos et al., 2011). Although, little attention has been drawn to the quantification of tsunami erosion in the nearshore area to date (Yoshikawa et al., 2015), Goto et al. (2011b) determined severely impaired stability of coastal infrastructures due to strong localized scouring and sediment rearrangement. Additionally, remarkable bathymetric changes caused by tsunamis have been numerically simulated (e.g., Orai Port, Japan (Kuriyama et al., 2020)) and observed in several nearshore areas (e.g., Kirinda Harbor, Sri Lanka (Goto et al., 2011b)), suggesting substantial sediment remobilization by tsunami waves in the shallow offshore area.

The particle entrainment by flows has been quantified from flume experiments (e.g., Mantz, 1977; Shields, 1936) and identified as being strongly dependent on the bed shear-stress, flow regime, as well as grain-size distribution, grain shape, grain packing, and density of the bed surface sediment (e.g., Boggs, 2014; Buffington & Montgomery, 1997). The resulting hydrodynamic description may be partially transferable to tsunami-induced sediment transport in shallow water (Kihara et al., 2012). Therefore, for the incipient motion of sediment particles by tsunami propagation, the fluid force, which consists of the bed-parallel drag force and the horizontal lift force, need to be larger than the resistance force of the particles to be moved (e.g., Lee & Balachandar, 2012; Van Rijn, 2007). Here, the Shields diagram that relates the dimensionless bed shear-stress and the grain Reynolds number, can be used for determining the threshold of sediment motion in uniform and non-uniform flows (Shields, 1936).

The main objective of this study is to find evidence for sediment remobilization in the Lucerne Bay caused by the 1601 CE tsunami in Lake Lucerne (Hilbe & Anselmetti, 2015; Schwarz-Zanetti et al., 2003) using sediment cores, lake-surface samples, and numerical simulations of tsunami wave propagation. First, we investigate the sedimentary properties in the Lucerne Bay through a series of collected sediment cores and modern lake-surface samples. Then we simulate tsunami generation by one of the largest subaqueous mass movements triggered by the 1601 CE earthquake and examine the simulated wave characteristics (water-surface displacement, and flow-velocity magnitude) and spatial extend of threshold conditions for incipient motion using the dimensionless bed shear-stress (Shields parameter) in the Lucerne Bay of Lake Lucerne.

2 Study Site

Lake Lucerne is a perialpine lake located in Central Switzerland at an altitude of 433.6 m above sea-level (m a.s.l). It geologically lies between the Helvetic nappes, the Subalpine Molasse, and the Swiss Molasse basin (Figure 1; Funk et al., 2013; Hantke et al., 2005; Kopp et al., 1955). The fjord-like lake consists of several subbasins with a maximum (max.) water depth of 214 m and predominantly steep-sided lakeshores.

Lucerne Bay is a relatively shallow subbasin in the eastern part of the lake with a water depth between 2.5 to 5 m (max. water depth 8 m) and a sharp transition in the west leading to deeper parts of the lake (Figure 2). The basin is glacially eroded into Burdigalian sandstones of the Upper Marine Molasse (UMM) and Aquitanian sandstones and conglomerates of the Lower

Freshwater Molasse (USM; Kopp et al., 1955; Schlunegger et al., 1997). The top of the bedrock occurs at a lowermost elevation of 408.8 m a.s.l at the lake outlet (Keller, 2020) and at ~335 m a.s.l at the Lucerne railway station in the southwest of the Lucerne Bay (Figure 2a; Keller, 2013). The up to 100-m-thick overlying Quaternary deposits consist of a sedimentary succession formed by a thick package of Late Pleistocene sediments characterized by glacially overconsolidated basal lodgment diamicts, and local esker gravels above the bedrock surface, which are overlain by heterolithic glaciolacustrine silts with sand lenses (Keller, 2020). Around 14’700 years Before Present (yr. BP), the area of the Lucerne Bay was filled with Late Pleistocene sediments up to 422 m a.s.l at the Lucerne railway station and up to 426 m a.s.l at the northern lakeshore (Keller, 2020). These sediments are overlain by a relatively thin (1–4 m) sequence of transgressive-regressive Holocene deposits that comprise shallow lake to alluvial plain deposits, peat-rich swamp deposits, carbonate mud, as well as deltaic deposits and gravelly lobes at the toe of incoming rivers (Keller, 2020). Major inflowing tributaries of the Lucerne Bay are the Würzenbach River in the northeast and the Krienbach River in the west, delivering dominantly siliciclastic material (Figure 2a). The Würzenbach, entering the lake at the northern shore, is today artificially canalized, but formed a large delta over time. In the southwestern area of the City of Lucerne, the Krienbach formed an extensive Holocene flood plain with gravelly alluvial fan deposits and overbank sands that repeatedly clogged temporarily the lake outlet caused high lake levels (Keller, 2013; Keller, 2020). Nowadays, the river is artificially diverted underground with tunnels feeding into the River Reuss, the main outflow of Lake Lucerne (Figure 1).

Lake level is relatively stable at 433.6 m a.s.l., with high lake levels in spring and late summer and low lake levels in winter and peak summer (BAFU, 2009). At the time of the city foundation (~1200 CE) lake-level was around 432.2 to 433.2 m a.s.l. (Keller, 2013). Through the construction of mills and a weir at the lake outlet in the 13th to 14th century, lake level was stabilized at 433.0 m a.s.l. (Keller, 2013). Prior to the historical record, lake level was presumably lower, with greater seasonal fluctuations (±1.5 m; Keller, 2020). In the Late Glacial Interstadial (~15’000–13’000 yr. BP), lake level was at ~432 m a.s.l (Keller, 2020) and during the Neolithic Period (5000–6000 yr. BP) lake was presumably lowest at around 428.6–429.5 m a.s.l. (Keller, 2013; Michel et al., 2012). After 1800 CE until today, strong artificial shoreline changes were carried out, especially around the City of Lucerne, but also around the lake in smaller villages.

2.1 The 1601 CE Earthquake and Lake Lucerne Tsunami

The 1601 CE earthquake with an epicenter in "Unterwalden", Central Switzerland (Mw ca. 5.9; Fäh et al., 2011; Schwarz -Zanetti et al., 2003) triggered multiple subaqueous mass movements (e.g., Hilbe et al., 2011; Siegenthaler et al., 1987; Schnellmann et al., 2002, 2006) and a subaerial rockfall (e.g., Keller, 2017; Schnellmann et al., 2006; Schwarz-Zanetti et al., 2003). All of these mass movements generated a basin-wide tsunami with wave heights exceeding 4 m and devastating inundation and run-up along the lakeshore (e.g., Cysat, 1969; Hilbe & Anselmetti, 2015). Several casualties caused by the tsunami waves were reported (Cysat, 1969). In the shallow Lucerne Bay, at the outflow of the lake, historical chronicles report a seiche with an amplitude of about 1 to 2 m and an initial period of 10 min. Its amplitude decreased with time but the seiche persisted for several days after the event (Cysat, 1969).

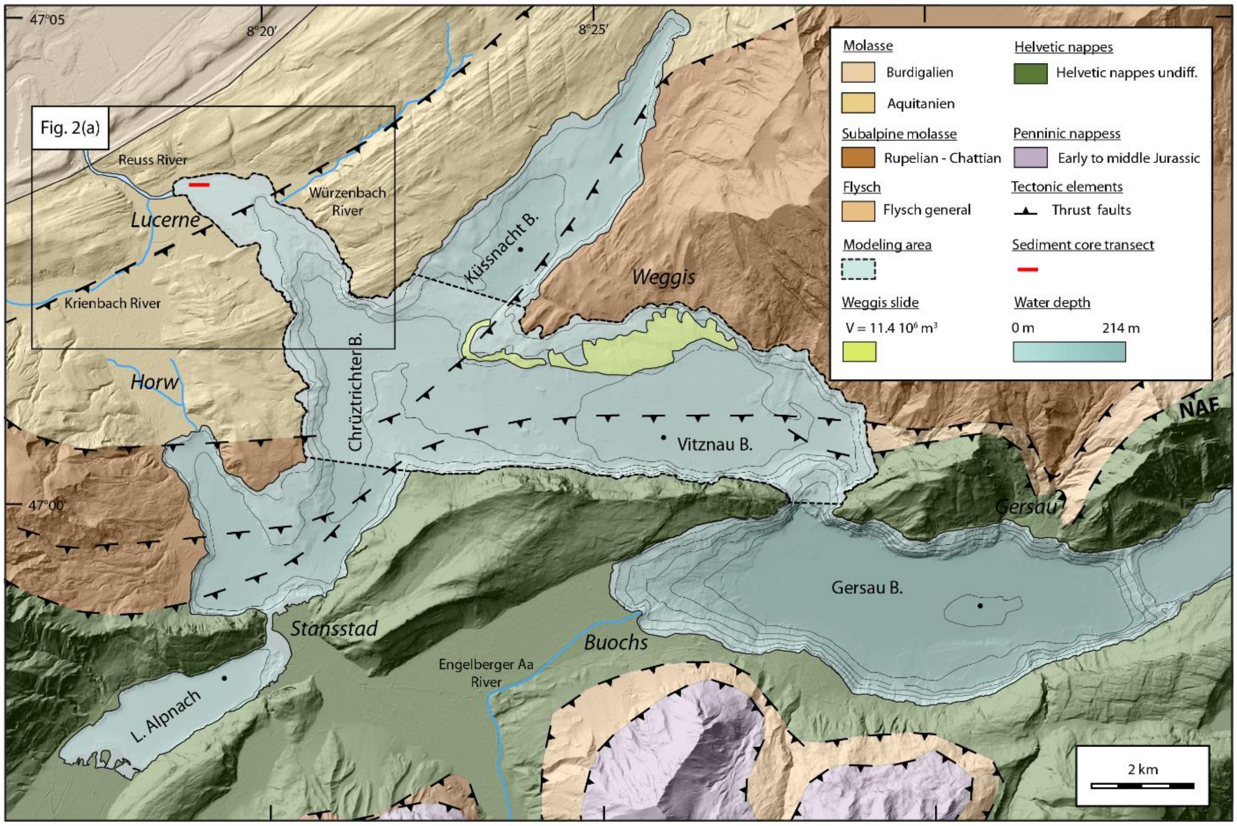

Figure 1. Western part of Lake Lucerne with individual lake basins (note that the Uri Basin in the east is not shown), extent of numerical simulation (light-blue area), dashed line indicating open weir boundary condition towards adjacent lake basins), and areal extent of the simulated Weggis-slide mass movement (yellow). The map is based on the swisstopo swissALTI3D digital terrain model, geological map of swisstopo (GK500-Geol) and the bathymetry map of Hilbe et al. (2011).

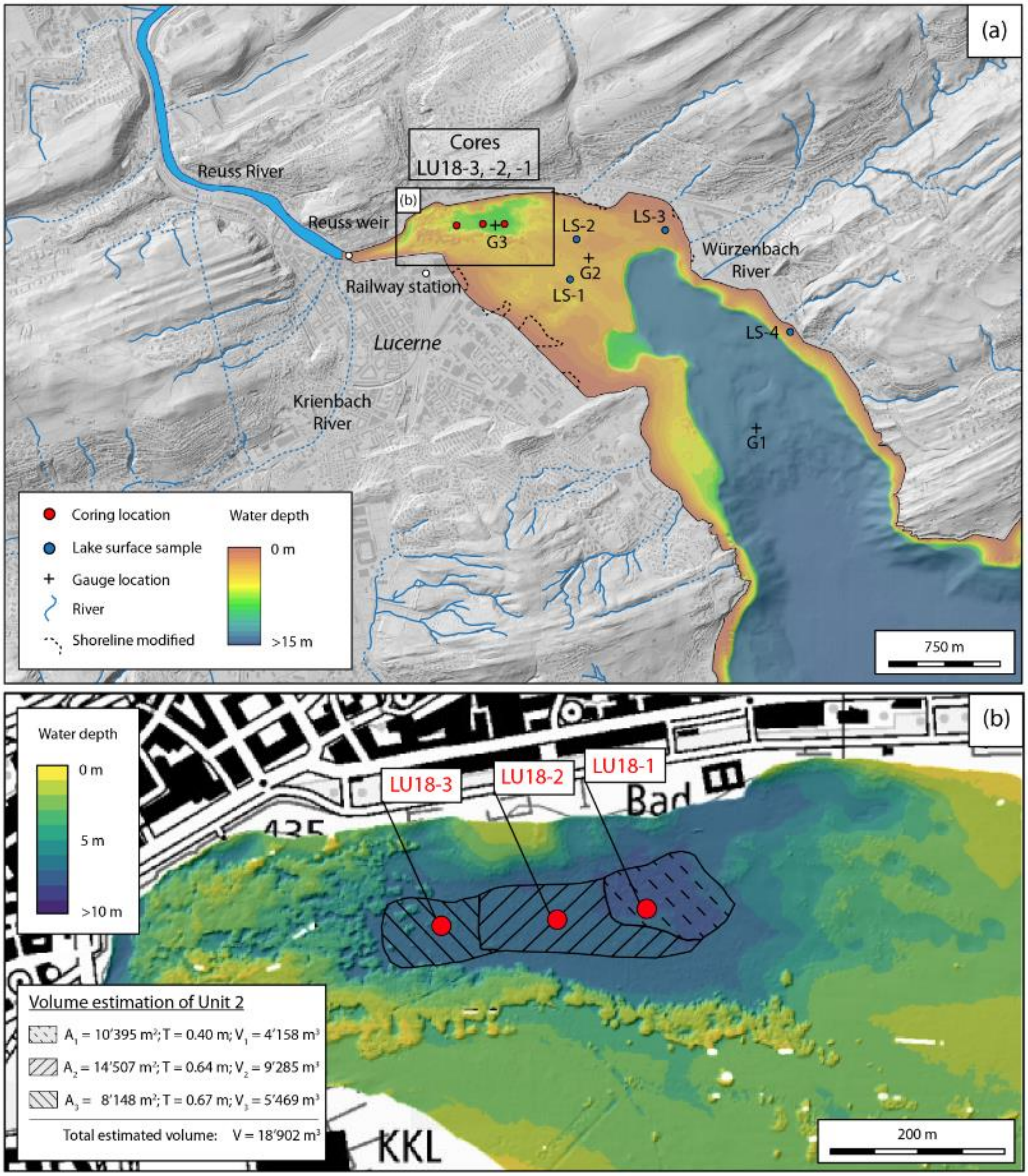

Figure 2. (a) Detailed map of the Lucerne Bay with the interpolated bathymetry (modified from Hilbe et al., 2011) used for the numerical simulation with its outline (solid black line) and artificial obstacles such as landfills and coastal infrastructure that were cut off (exact shoreline course: dashed line). The map is based on the swisstopo digital terrain model swissALTI3D and the national map LK50 from swisstopo. The sediment core location (red dots), sediment core ID (red), surface sediment samples (blue dots) and virtual gauges (black crosses) plotted in Figure 9 are shown. (b) Detailed high-resolution bathymetric map (Hilbe et al., 2011) of the east-west

oriented depression shows the location of the sediment cores (red dots) and the area (black shaded) used for the volume estimation of the siliciclastic-rich, normally graded Unit 2. The shallowest and rugged topography represents artifacts caused by aquatic plants.

3 Methods

3.1 Sedimentological Investigations

High-resolution (1 m grid cell) bathymetrical data of Lake Lucerne (Hilbe et al., 2011) were used for the coring-site selection (Figure 2b). Three sediment cores (Core LU18-1, -2, and -3) were recovered from a floating platform in water depth between 7 to 8 m (Figure 2b) with a 3-m-long percussion piston-coring system (UWITEC Co. Austria) up to a subsurface depth of 3.5 m. A gravity corer was used to recover the undisturbed water-sediment interface. The observed lithological units are visually correlated. Lake-surface samples were collected at four locations along the Lucerne Bay.

3.1.2 Sediment Cores

Petrophysical properties (bulk density gamma-ray attenuation, magnetic susceptibility, and p-wave velocity) were measured on all recovered whole round cores with a Geotek multi-sensor core logger (MSCL-S). Whole round cores also underwent X-ray computed tomography (CT) imaging using a medical Siemens Somatom Definition AS scanner. Full core CT-scan data were obtained at a voxel size of 100 µm and visualized with the RadiAnt DICOM Viewer software (version 4.6.9.18463). Sediment cores were split longitudinally, imaged with the MSCL-S core logger line-scan camera, and sedimentologically described. A complete composite sediment record was obtained by visual correlation of overlapping piston and gravity cores. High-resolution assessment of sediment geochemistry by means of X-ray fluorescence (XRF) scanning was performed on split core surfaces of Core LU18-2 with an ITRAX-XRF core scanner (Cox Ltd., Sweden). Measurements were performed with a Cr-tube set to 30 kV and 50 mA using longitudinal 2 mm integrals and 20 s integration times. Here we report relative intensities of calcium (Ca) and silicon (Si) to aluminum (Al) and titanium (Ti), respectively.

Sediment samples were continuously taken at 10 cm intervals in Unit 1 and 2 (Core LU18-2) and at 1 cm intervals in Unit 3 (Core LU18-1). Only two subsamples were taken from the top of Unit 4 (Core LU18-1) due to its presumably glacio-lacustrine sediment appearance. All sediment subsamples were freeze-dried and homogenized using mortar and pestle. Total carbon (TC), total nitrogen (TN) and total sulfur (TS) concentrations were measured on these samples with a Flash 2000 NCS (Thermo Fisher Scientific Co.) flash combustion elemental analyzer configured with a MAS plus autosampler (Thermo Fisher Scientific Co.) and thermal conductivity detector. For analysis samples were weighed into tin (5–8 mg) capsules for TC, TN, and TS measurements and silver (4–5 mg) capsules for total organic carbon (TOC) measurements. For TOC concentration measurements samples were treated with 1M HCl until no visual reaction occurred. The remaining HCl was evaporated prior to flash combustion analysis. Total inorganic carbon (TIC) was calculated from the differences between TC and TOC. The molar carbon-to-nitrogen (C/N) ratio was determined from TOC and TN concentrations. $CaCO_3$ was calculated from TIC using the stoichiometric conversion factor of 8.33.

A sandy deposit (Unit 2) was continuously subsampled at 1 cm intervals between 37 and 120 cm depth in Core LU18-2 for grain-size analysis. Subsamples with a wet weight of 1 g were treated with 10%vol HCl and 10%vol H_2O_2 to remove solid carbonate species and organic matter. A dispersion solution containing $Na_6P_6O_{18}$ and Na_2CO_3 was added to the remaining clastic fraction and shaken in aqueous suspension for an 1 h prior to analysis. Laser diffraction analysis (LDA) was then carried out with a Malvern Mastersizer 3000 particle size analyzer. Volume percentages (%vol) was calculated for each sample from the average of 3 aliquot measurements. Grain-size classes are presented after the classification proposed by Wentworth (1922).

Radiocarbon dating of terrestrial plant macro-remains from Core LU18-2 was used to date a sandy deposit (Unit 2). In total 6 samples were measured by accelerator mass spectrometry (AMS) with the Mini RadioCarbon Dating System (MICADAS) at the Department of Chemistry and Biochemistry, University of Bern. Radiocarbon ages were calibrated into calendar years Common Era (cal CE) using the OxCal software (version 4.3; Ramsey 2009) and the IntCal20 Northern Hemisphere calibration curve (Reimer et al. 2020).

3.1.2 Lake-Surface Sediment

Lake surface samples (uppermost ~10 cm) were collected by diving with a shovel and a bucket during summer from a sailboat. The collected lake-surface sediment samples (Figure 2a) were described macroscopically using a binocular. Total carbon, TN, TS, and TOC concentrations were measured, and TIC and $CaCO_3$ concentrations as well as the molar C/N ratio was calculated according to the procedure described above. For the grain-size analysis the same procedure as described in the previous section was performed.

3.1.3 Estimation of sediment volume for Unit 2

The depositional volume of Unit 2 was estimated based on the high-resolution bathymetric data from Hilbe et al. (2011) and the thickness of Unit 2 observed in sediment cores. Polygons of the estimated areal extent of the sediment packages were drawn, and the area was calculated using ArcMap (version 10.8.1). Due to high gas content of sediment in the Lucerne Bay area, previously acquired seismic reflection data could not be used to characterize the spatial distribution of sedimentary units.

3.2 Numerical Simulation, Visualization, and Sensitivity Analysis of the Bed Shear-Stress

The wave generation, propagation, and inundation were numerically simulated with the software BASEMENT (BAsic-Simulation-EnvironMENT). The software, originally designed for quasi-1D and 2D simulations of river hydro- and morphodynamics in alpine and subalpine regions (Vanzo et al., subm.), has been recently validated for the hydrodynamic modelling of tsunami waves on lakes.

BASEMENT is a freeware (www.basement.ethz.ch). The numerical modelling tool is used in academic research as well as engineering practice and provides a user-friendly environment for study of manifold problems. It enables the simulation of steady and unsteady hydraulic flow conditions with complex geometries as well as sediment transport. The underlying mathematical description is based on a decoupled system of equations given by the 2D-depth averaged non-linear shallow-water model for the hydrodynamics and the Exner equation for morphodynamical modelling. Finite volume spatial discretization in combination with Riemann solver guarantees the stability and robustness of the numerical solution (Vetsch et al., 2020). Due to its highly optimized design, the software allows for accelerated simulations using multi-core CPUs, GPUs (graphic processing unit), and hybrid CPU-GPU. For hydrodynamic simulations, BASEMENT computes water-surface elevation h and specific discharges q_x and q_y in a selected computational domain. From these quantities, the water-surface displacement

$$A = h - h_{ref},$$

with h_{ref} initial still water reference-level and the flow-velocity magnitude

$$u = \frac{\sqrt{q_x^2 + q_y^2}}{h}$$

can be derived (Figure 3).

The bed shear-stress is defined as

$$\tau = \frac{u^2 \rho_f}{c_f^2},$$

with ρ_f fluid density, c_f friction coefficient for fully turbulent flow computed according to Chézy as

$$c_f = 5.75\ \log(12\frac{h}{k_b})$$

(e.g., Bobrowsky & Marker, 2018) and bed roughness (k_b), which may range from grain roughness to total physical bed-roughness as mentioned in Houwman & van Rijn (1999). The dimensionless form of the bed shear-stress derived by Shields (1936) based on dimensional analysis (also known as the Shields parameter) is defined as

$$\theta = \frac{\tau}{(\rho_s - \rho_f) g d_s},$$

where ρ_s represents the sediment density, g the gravitational acceleration and d_s the grain diameter of bed surface sediment.

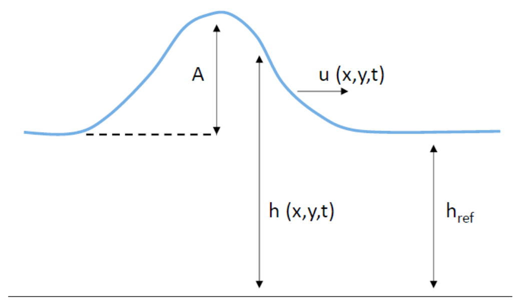

Figure 3. Sketch of computed numerical quantities: initial still-water reference-level (h_{ref}), water-surface elevation (h), water-surface displacement (A) and flow-velocity magnitude (u).

The considered computational domain is limited to the Vitznau Basin and the Lucerne Bay with open boundaries (non-reflective boundary condition) to allow a natural outflow towards the Gersau, Küssnacht, and Horw Basins and at the lake outlet in the Lucerne Bay (Figure 1). The digital elevation model is based on the high-resolution bathymetric data obtained by Hilbe et al. (2011), which was resampled to a cell size of 25 m^2. Shallow-water areas (water depth 0–4 m), which are not entirely covered by the bathymetrical data were linearly interpolated to the current shoreline, whereas large artificial obstacles (islands and port facilities) were cut out (Figure 2). From the resampled bathymetry, the computational grid with 787.4k triangular elements with an average cell size of 115 m^2 in the central Vitznau Basin and 25 m^2 in the Lucerne Bay area was created. Details on the computational performance are summarized in Table 1 to allow an estimation on the computing time requirements for the numerical simulation performed.

The initial volume of the mass movement was taken from the bathymetric reconstruction prior to the 1601 CE earthquake (Hilbe & Anselmetti, 2015). The initial displacement of the water column caused by the "Weggis-slide", was modelled with an instantaneous downward vertical displacement of the identified area by 5 m (2.3 km^2 area with a total failed volume of 11.4 x 10^6 m^3; Figure 1).

Table 1. Details of the numerical set-up and performance of the simulation via BASEMENT.

number of mesh elements	element area range [m^2]	simulation time [s]	computing time [s]	GPU card
787.4k	25-115	1800	312	TeslaP100-PCIE-12GB

Data visualization was performed with the numerical data visualization software Paraview (V5.8.1, www.paraview.org). Three virtual gauges were placed in the Lucerne Bay:

gauge 1 is located at the entrance of the Lucerne Bay, gauge 2 in the shallow-water area and gauge 3 in the east-west oriented depression (Figure 2a). Time series of water-surface displacement, flow-velocity magnitude, specific discharge, bed shear-stress and dimensionless bed shear-stress (Shields parameter) were investigated using gauge data (Figures S1, S2, and S3). In addition, the spatial variability of the variables at different time steps was analyzed on map scale. Flow-field vectors were used to reconstruct the flow path and direction of potential sediment transport.

4 Results

4.1 Lake-Surface Sediments

The lake-surface sediment samples (Table 2) are characterized as carbonate mud with coarse organic remains (Sample LS-1 and LS-2), poorly sorted siliciclastic sand with fine gravel and carbonate shells (Sample LS-3), and a mixture of siliciclastic fines and carbonate mud with coarse organic remains (Sample LS-4). Sample LS-1 and LS-2 are collected in the central part of the Lucerne Bay (Figure 2A). Sample S-3 is taken in the western part of the Würzenbach river delta, and Sample LS-4 on the northeastern lakeshore of the Lucerne Bay (Figure 2a; see Supporting Information SI for coordinates of the sample location (Table S1) and results of the CNS measurements (Table S2)).

Table 2. Lake-surface sediment samples collected in the shallow area of the Lucerne Bay: sample ID, macroscopic description, TOC and $CaCO_3$ concentrations, molar C/N ratio, D_{50} of the grain-size distribution as well as the volume percentage of the clay-, silt- and sand fraction.

Sample ID	Macroscopic description	TOC (wt.%)	$CaCO_3$ (wt.%)	C/N ratio (mol mol^{-1})	D_{50} (µm)	Clay (vol.%)	Silt (vol.%)	Sand (vol.%)
LS-1	Carbonate mud with coarse organic	2.208	80.8	6.7	45	3	60	37
LS-2	Carbonate mud with coarse organic	2.424	78.4	6.8	58	3	50	47
LS-3	Poorly sorted siliciclastic sand with fine gravel	0.427	5.1	7.5	340	0	3	97
LS-4	Carbonate mud with coarse organic	2.481	26.9	9	45	3	62	35

4.2 Sediment-Core Data

Based on high-resolution bathymetric data (Hilbe et al., 2011) a topographic depression was identified in the Lucerne Bay near the lake outlet (Figure 2b). The depressional feature is characterized by an east-west oriented longitudinal shape with a length of ~400 m and width of ~200 m, and an average water depth of 7.5 m, while the surrounding plateau of the Lucerne Bay has a water depth of ~3.5 m. This depression surrounded by shallow water provide an ideal depositional environment suitable for trapping remobilized sediment from tsunami inundation and backwash. Three sediment cores (LU18-1, LU18-2, and LU18-3) were retrieved along an east-west oriented transect within the depression to study sedimentary composition and structures (see Supporting Information SI for coordinates of core location (Table S3).

Recovered sediment cores have a complete composite sediment record of 284 cm (Core LU18-1); 288 cm (Core LU18-2) and 218 cm (Core LU18-3). The lithostratigraphy consist of four well-traceable sedimentary units (Figure 4) observed along the offshore sediment core transect (Figure 5), which were identified by visual appearance and core-log data (see Supporting Information SI (Table S4) for CNS measurements in Unit 1, 2, 3, and 4).

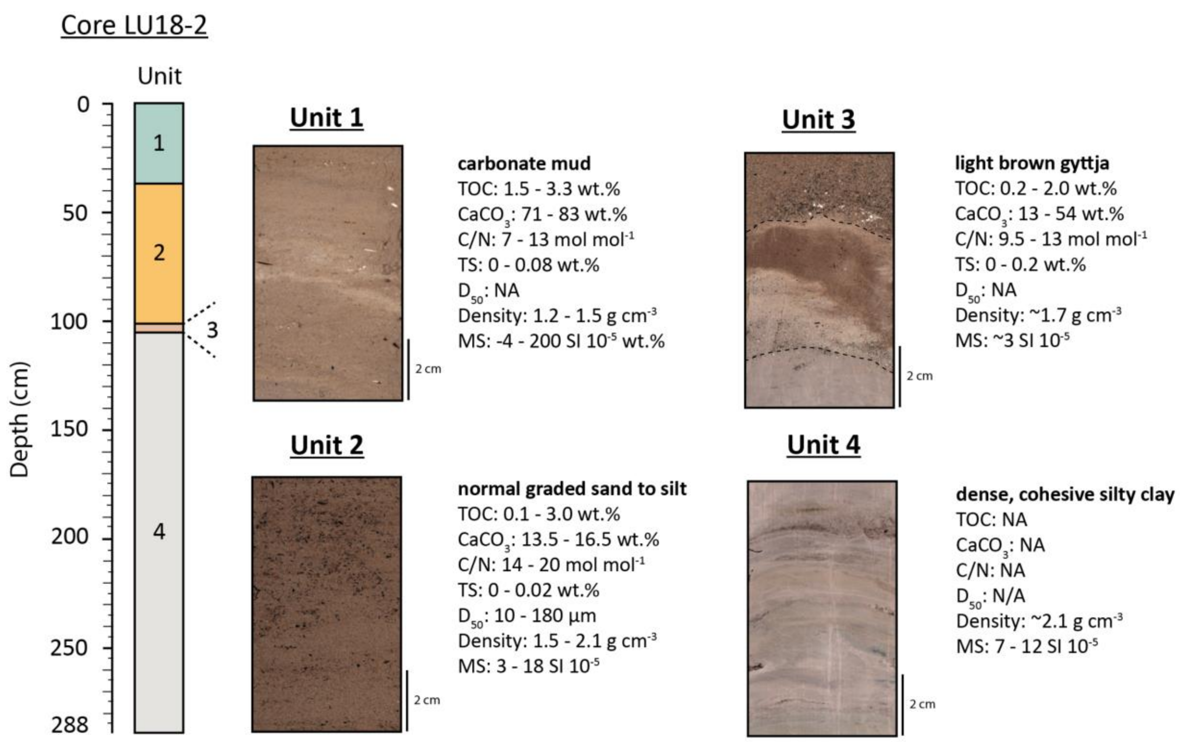

Figure 4. Complete composite sediment Core LU18-2, selected line-scan images of the four lithologic units, and its sedimentologic properties (TOC, $CaCO_3$ and TS concentrations, as well as molar C/N ratio, D_{50} of the LDA grain-size distribution, density, and magnetic susceptibility (MS)). Note that in the line-scan image of Unit 3, the lower gradual contact and upper sharp contact are indicated with a dashed black line.

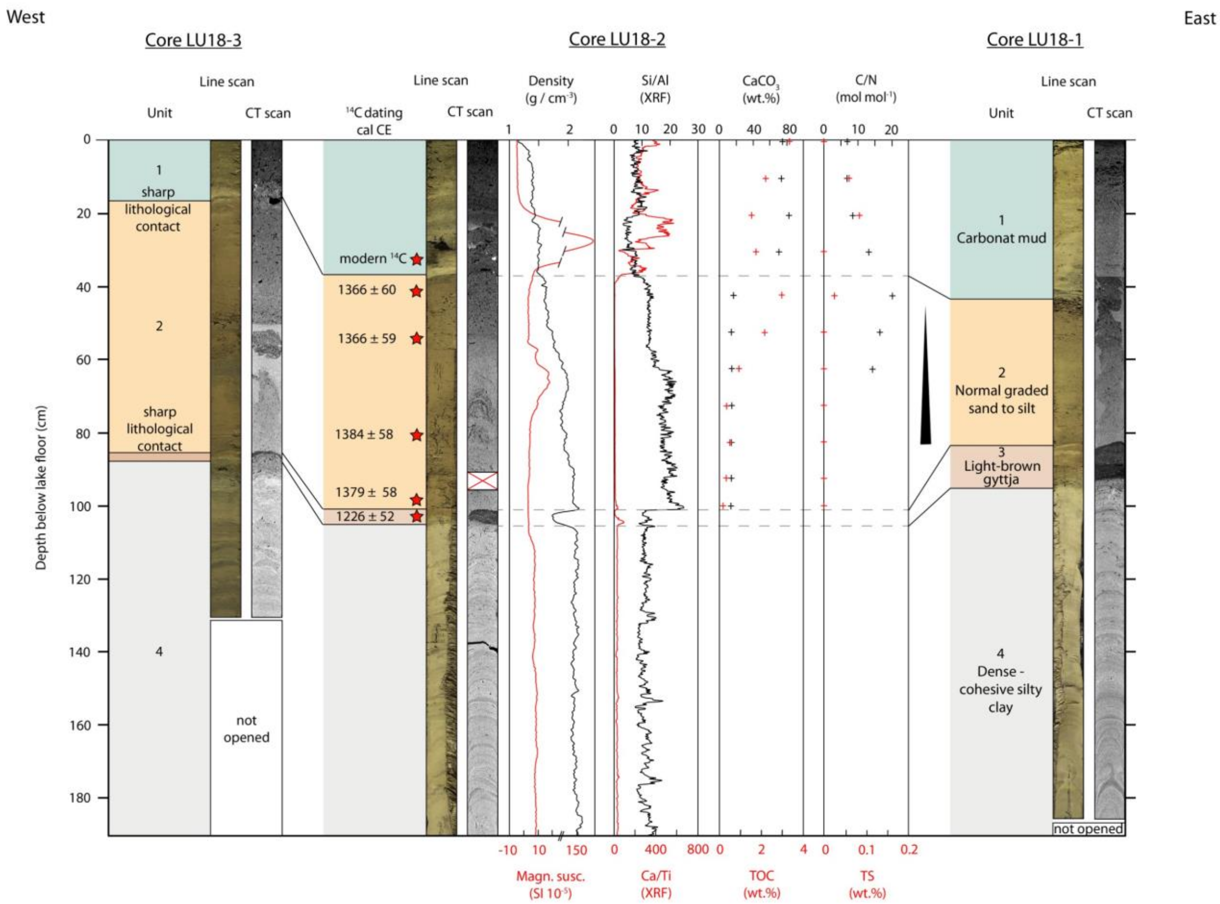

Figure 5. Sediment core transect of core LU18-1, -2, and -3 recovered along the east-west oriented depression in the Lucerne Bay (Figure 2b). The sedimentological transect overview shows calibrated radiocarbon ages, sedimentary units, line-scan images, CT-grayscale images, density, magnetic susceptibility (Magn. susc.), Si/Al- and Ca/Ti ratio from the XRF scans, $CaCO_3$, TOC and TS concentrations, and molar C/N ratio (see Figure 7 for results of Unit 3).

4.2.1 Sedimentary Unit Description

4.2.1.1 Unit 1: Carbonate Mud

Unit 1 is light gray in color, varies in thickness between 17 and 43 cm, consists of shell fragments embedded in an endogenous carbonate mud matrix, with siliciclastic minerals only as accessories. It has a $CaCO_3$ concentration of 70–80 wt.%, a gradual downcore decrease in TOC (3.3–1.5 wt.%), and an increase in the C/N ratio (7–13 mol mol^{-1}) and density (1.2–1.5 g cm^{-3}; Figure 5). Magnetic susceptibility is slightly negative in the upper 20 cm (-4 SI 10^{-5}) and has a peak at 27.5 cm depth (197.5 SI 10^{-5}), which is due to metallically shiny, black, gravel-sized coal particles.

4.2.1.2 Unit 2: Normal Graded Sand to Silt

Unit 2 is dark brown in color and consists of a thick (40 to 67 cm), dense, siliciclastic normal graded fine to medium sand with sharp lower and upper contacts and four internal subunits (Subunit 2_A to 2_D; Figure 6). Coarse sand-sized shell fragments are finely dispersed in a fine siliciclastic sand at the bottom of the 40 to 67 cm thick normal graded sand to silt deposit with sharp lower and upper sedimentary contacts observed by sediment core line scan and CT grayscale images (Figure 5). The enrichment of macroscopically observed carbonate shell fragments at the bottom is also expressed in the distinct XRF Ca/Ti ratio peak at the base (Figure 5). In the upper part, carbonate is homogeneously present (13.5–16.5 wt.%) and is occasionally found as fine sand-sized shell fragments. The C/N ratio (14 to 20 mol mol^{-1}) could only be calculated in the top three subsamples at 40, 50, and 60 cm core depth, but not in the lower subsamples due to nitrogen concentrations below detection limit (Figure 5). The high C/N ratio fits well to the large amount of macroscopic, horizontally embedded wood fragments, whose abundance decreases toward the base. Magnetic susceptibility ranges from 3 to 18 SI 10^{-5}, and density increases downcore from 1.5 to 2.1 g cm^{-3} (Figure 5). Similarly, the mean grain size (D_{50}) and sorting increases downcore from poorly to moderately sorted silt to well sorted fine sand (Figure 6). Four subunits were identified from the LDA grain-size data (2_A (37-55 cm), 2_B (55-60 cm), 2_C (60-95 cm) and 2_D (37-55 cm)), which are grouped based on their mean grain-size (D_{50}) and grain-size distribution. The XRF Si/Al ratio correlates well with the LDA grain-size data and can be used as grain-size indicator (Figure 5).

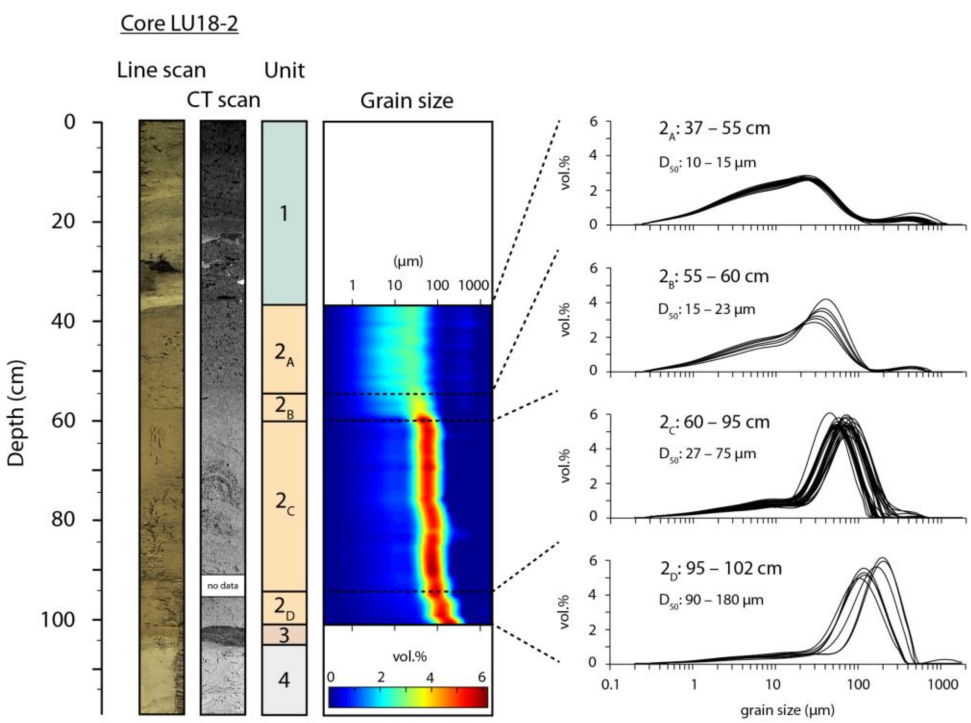

Figure 6. Line-scan image, CT-grayscale image, and particle-size distribution from the LDA of Unit 2 in Core LU18-2. The grain-size distribution of the siliciclastic fraction shows a pronounced fining upward trend in Unit 2, which is divided into 4 subunits (Subunit 2_A to 2_D).

4.2.1.3 Unit 3: Light Brown Gyttja

Unit 3 is a light brown gyttja with occasional beige laminae, variable thickness between 2 to 10 cm with coarse sand and carbonate shell fragments embedded in an organic-rich matrix with low density (1.7 g cm^{-3}), and a gradual transition over > 2 cm at the base (Subunit 3_T). The low density of the unit is well pronounced in the CT grayscale image, which has sand-sized particles (siliciclastic grains as well as complete and fragmented carbonate shells) embedded in an organic matter-rich matrix (Figure 7). Total organic carbon is high (1.5–2 wt.%) in the upper part (83–91 cm) and decreases to ~0.2 wt.% at the base of the unit. The C/N ratio varies between 9.5 to 13 mol mol^{-1} and sulfur is present (0–0.2 wt.%). $CaCO_3$ varies between 13–54 wt.% and is highest within the beige laminae. Magnetic susceptibility is ~3 SI 10^{-5}. A gradual transition with variable thickness along the sediment-core transect is evident at the base of the unit on the CT grayscale image (Figures 5 and 7). The transitional base of Unit 3 is brownish gray in color and consists of fine to medium sand with carbonate shell fragments (Figure 5) and a distinct peak in the XRF Ca/Ti ratio (Figure 5).

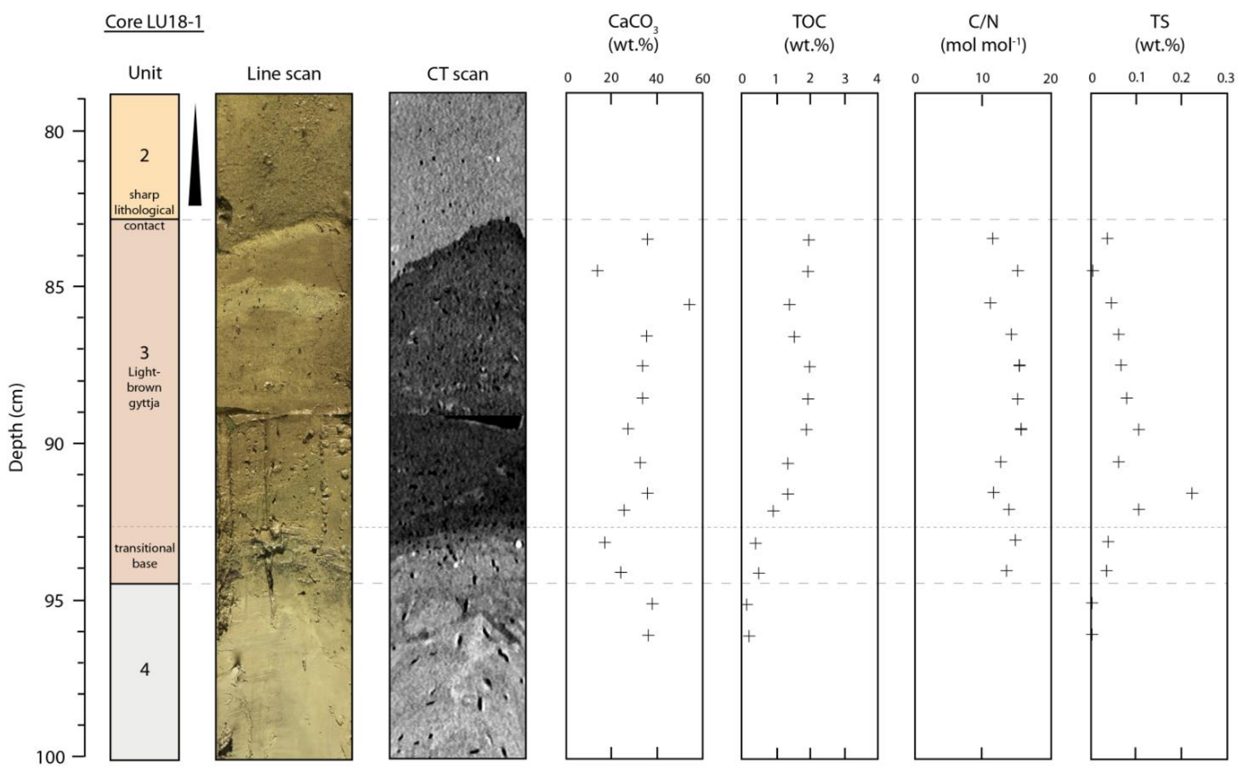

Figure 7. Line-scan image, CT-grayscale image, $CaCO_3$, TOC and TS concentrations, and the molar C/N ratio of subsamples from Unit 3, its lower transitional base and the uppermost of Unit 4 in Core LU18-1. The sharp basal contact of Unit 2 is well recognizable in the CT-grayscale image.

4.1.2.4 Unit 4: Dense – Cohesive Silty Clay

Unit 4 is light gray in color and consists of a cohesive, very dense (~2.1 g cm^{-3}) silty, clay-rich sedimentary deposit. Magnetic susceptibility varies only slightly within the unit (7–12 SI 10^{-5}). Fine laminae of variable thickness and graded fine sand to silt are well recognizable on CT grayscale images (Figure 5). These graded intervals are also well expressed in the XRF Si/Al ratio that may be used as grain-size indicator (Figure 5).

4.3 Radiocarbon Dating

Four radiocarbon dates obtained from terrestrial organic macro remains found in Unit 2 have calibrated radiocarbon ages in the range of 1306–1442 cal CE (Table 3, Figure 5). The four samples were collected at regular intervals throughout the unit. One sample of fragmented leaves from Unit 3 yields a radiocarbon age of 1174–1277 cal CE. Another sample of leaf fragments in Unit 1 has a modern radiocarbon age (Table 3). The calibrated radiocarbon age ranges presented are given within a 2σ confidence level, which corresponds to a 95.4% probability.

Table 3. AMS radiocarbon age and $\delta^{13}C$ results from terrestrial organic macro remains from Core LU18-2. Radiocarbon age uncertainties refer to 1-sigma uncertainties. Range of calibrated represent 95.4% probability (2σ).

Sample	Core depth (cm)	Sample material	$\delta^{13}C$ (‰)	14C age ± 1σ (14C years BP)[a]	Calibrated 2σ range (cal CE)[b]
BE-10751.1.1	35–36	Leave fragments	-28.7	-572 ± 31	Modern
BE-10752.1.1	41–42	Conifer needle	-28.7	570 ± 31	1306–1425
BE-10753.1.1	54–55	Conifer needle	-28.8	567 ± 30	1307–1425
BE-10754.1.1	79–80	Conifer needle	-27.4	527 ± 31	1326–1442
BE-10755.1.1	98–99	Leave fragments	-31.8	544 ± 30	1321–1437
BE-10756.1.1	102–103	Leave fragments	-29.7	812 ± 36	1174–1277

[a] Stuiver & Polach (1977); [b] Ramsey (2009); [b] Reimer et al. (2020).

4.4 Volume Estimation of Unit 2

The estimation of the total volume of Unit 2 along the east-west oriented depression is based on high-resolution bathymetrical data and retrieved sediment cores. Three polygons with areas of 10’395 m^2, 14’507 m^2 and 8’148 m^2, with a corresponding thickness of 0.4 m, 0.64 m, and 0.67 m, respectively, yield an estimated total depositional volume of 18’902 m^3 (Figure 2b; Table S5).

4.5 Numerical Tsunami Model

4.5.1 Tsunami Generation and Propagation

The 1601 CE Weggis-slide collapse with a volume of 11.4 x 10^6 m^3 (Hilbe & Anselmetti, 2015) was simulated by an instantaneous collapse of a 5 m thick sediment drape located on the northern lateral slope of the Vitznau Basin (Figure 1). This moving slab and the affected area (>

2 km^2) correspond to the well-defined 1601 CE Weggis-slide described by Schnellmann et al. (2005) and Hilbe et al. (2011). The numerically simulated wave generation and propagation can be divided in three phases: wave generation (phase 1), wave propagation in the Vitznau Basin (phase 2), and arrival of a first wave trough in the Lucerne Bay that is followed by 3 main wave pulses (phase 3). See Supporting Information SI for the animation of the wave proapagtion (Movie 1).

A wave trough with a water-surface displacement with respect to the lake at rest of more than -3 m forms immediately after the instantaneous collapse along the failed area (Figure 8a). After 20 s (Figure 8b) the first waves reach the nearest shore in the Gersau area with wave crests of 2 m forming after 40 s (Figure 8c). The tsunami wave reaches the steep southern shore within 60 s (Figure 8d) and is reflected towards the Vitznau Basin. A complex wave pattern is formed along the northern shoreline (Figure 8e and 8f). In the initial phase, a wave trough approaches the shore (after 10 s), which is followed by a long lasting spatially heterogeneous wave crest with water-surface displacements up to 2 m (from 40 to 140 s), until the reflected wave trough from the southern shore superposes the established wave crest (after 140 s).

Figure 9 shows four time-snapshots of the computed tsunami propagation and water-surface displacement in the Lucerne Bay. A train of waves arrives in the narrow and shallow Lucerne Bay with an initial wave trough and a water-surface displacement of up to -1 m after 410 s (Figure 9a). At the transition from the deeper to the more shallow-water area of the Lucerne Bay, a strong surge occurs in the direction of the wave trough with a flow-velocity magnitude greater than 2 m s^{-1}. At ~550 s (Figure 8b) the first wave crest with a water-surface displacement between +0.2 and +0.5 m inundates the bay with a bore-like appearance and max. flow-velocity magnitudes of 2.2 m s^{-1} at the wave front. The second wave trough is characterized by a complex and heterogeneous flow field, which inundates the bay at ~755 s (Figure 8c). The second wave crest has an impressive bore-like wave (Figure 8d) with an initial wave trough of -1 m and a following wave crest of +0.5 m (Figure 10a) and a max. flow-velocity magnitude of ~2.4 m s^{-1} at gauge 1 and ~0.9 m s^{-1} at gauge 3 (Figure 10b). The third wave has a smaller water-surface displacement than the first two, but flow-velocity magnitudes reached at gauges 2 and 3 are similar (Figure 10b). The third wave is followed by waves with smaller water-surface displacements and flow-velocity magnitudes (Fig 10a).

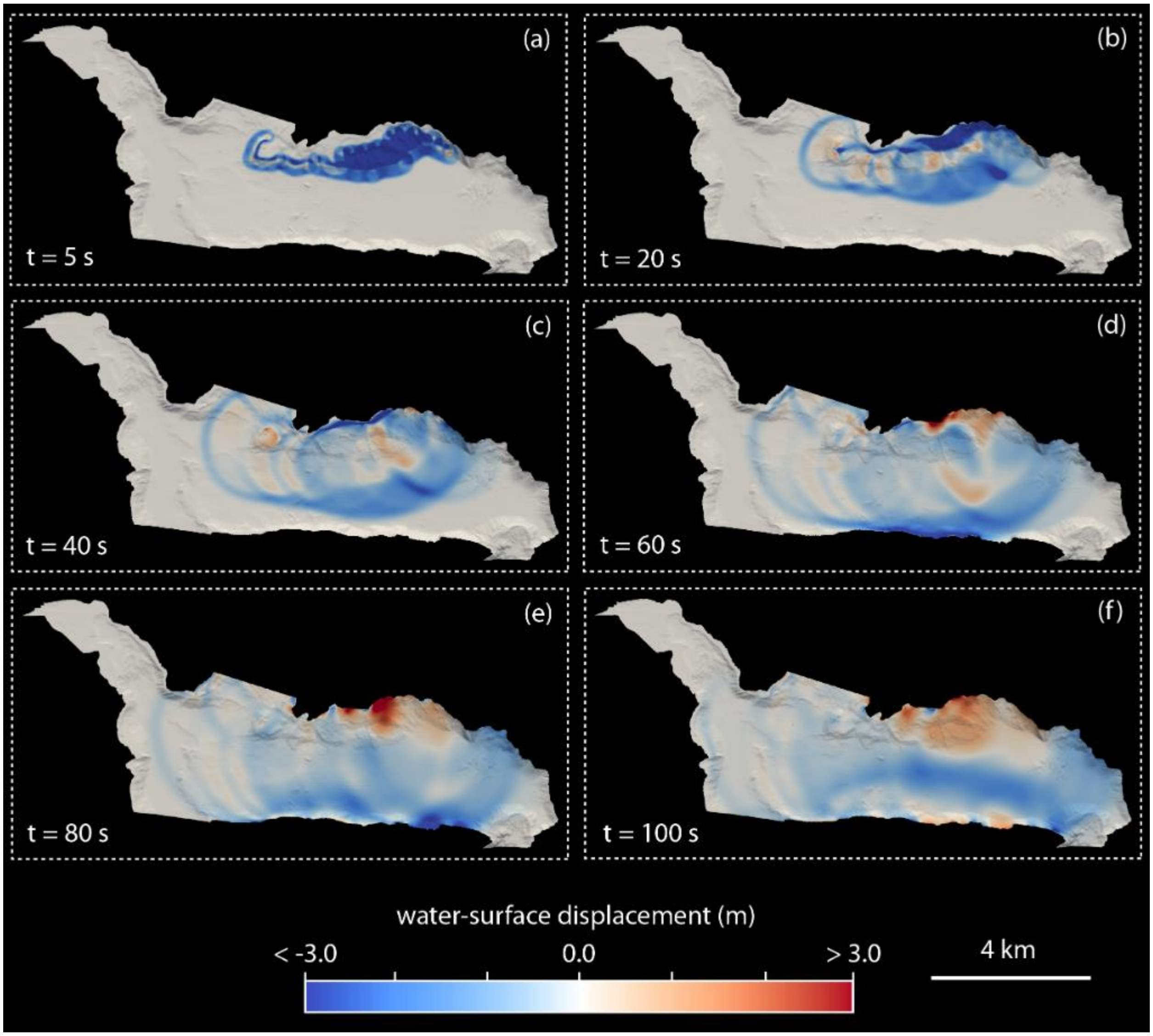

Figure 8. Time snapshots of the computed tsunami propagation and water-surface displacement (-3 to +3 m with respect to the lake at rest) of the 1601 CE Weggis-slide (simulation LU18-S4) within the first 100 s after the simulated slope collapse.

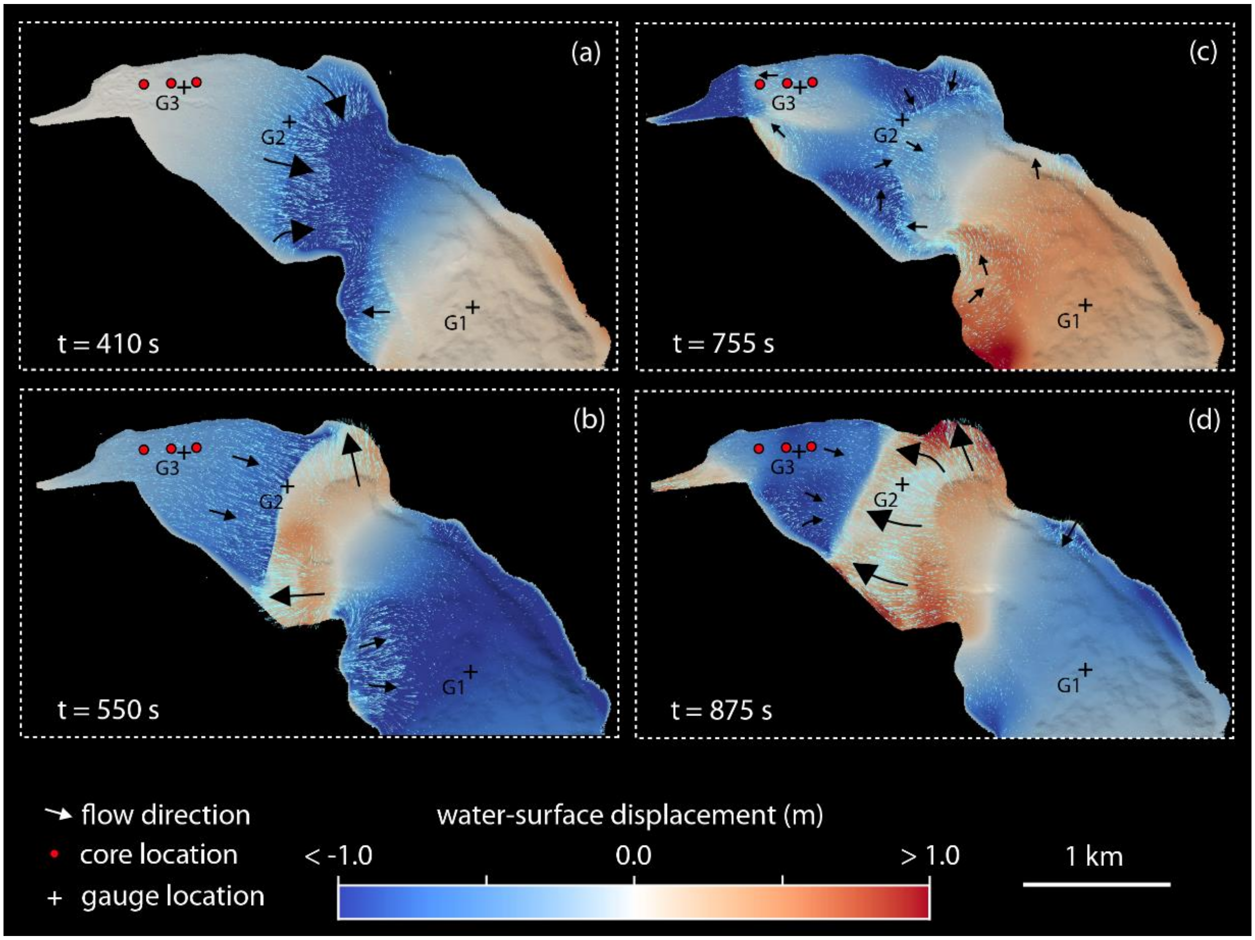

Figure 9. Time snapshots of the computed tsunami propagation and water-surface displacement of the 1601 CE Weggis slide (simulation LU18-S4) in the Lucerne Bay. The water-surface displacement (-1 to +1 m) and flow-velocity direction (black arrows redrawn for better visualization of actual model data indicated with fine, light-blue arrows) are shown at four distinct time steps (410 s, 550 s, 755 s, and 875 s). Time series of water-surface displacement and flow-velocity magnitude at the virtual gauges 1, 2, and 3 (black crosses) are plotted in Figure 10. Core locations (red dots) are shown in the map.

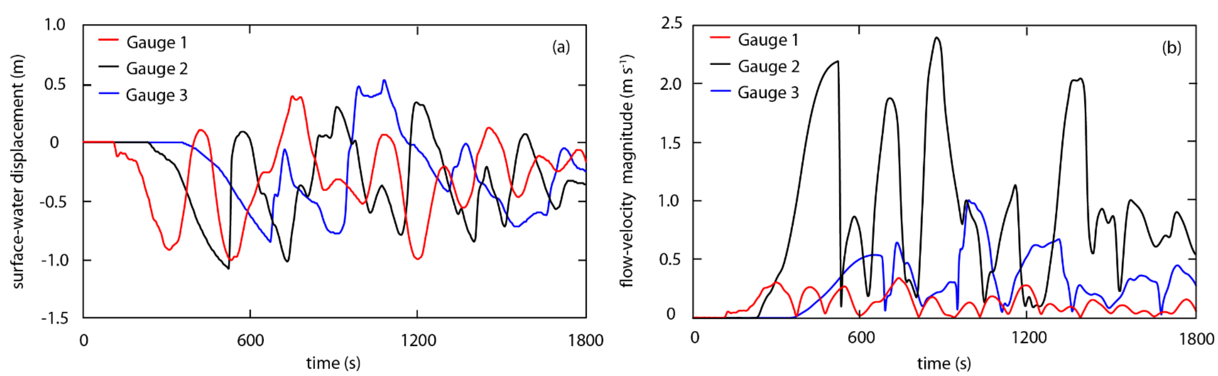

Figure 10. Timeseries of water-surface displacement (a) and flow-velocity magnitude (b) at gauges 1–3 (see Figure 9 for location) of the simulation LU18-S4.

4.5.2 Sensitivity Analysis of the Bed Shear-Stress

To determine the dependency and robustness of the computed flow parameters, a sensitivity analysis of the bed roughness k_b was performed. Six scenarios were simulated with different bed roughness values (k_b) ranging from 0.0002 to 0.1 m (Table 4). The sensitivity of the bed roughness (k_b) on the dimensionless bed shear-stress (θ) was evaluated by simulations computed with different bed roughness values (k_b) between 0.0002 and 0.1 m, keeping fluid density (1 g cm^{-3}), sediment density (2.65 g cm^{-3}), and sediment porosity (0.4 vol%) constant (Table 4). The area with a dimensionless bed shear-stress $\theta \geq 0.03$ (Table 4) was calculated with ArcMap (version 10.8.1).

Table 4. Sensitivity analysis of the dimensionless bed shear-stress to the bed roughness (k_b): applied bed roughness in the different scenarios computed with BASEMENT and the calculated area with a dimensionless bed shear-stress $\theta \geq 0.03$.

	LU-S1	LU-S2	LU-S3	LU-S4	LU-S5	LU-S6
Bed roughness k_b (m)	0.0002	0.001	0.01	0.02	0.06	0.1
Area with $\theta \geq 0.03$ (10^6 m^2)	0.20	0.28	0.38	0.43	0.52	0.57

The analysis of the computed data on map-scale and gauge data indicates that the applied bed roughness k_b has a strong effect on the dimensionless bed shear-stress. However, water-surface displacement, flow-velocity magnitude, and specific discharge are hardly affected. For example, flow-velocity magnitude has a variance of less than 10% within the range of the different simulations at gauge locations. Whereas the computed dimensionless bed shear-stress is strongly influenced by the applied bed-roughness coefficient as shown in Figure 11.

The max. dimensionless bed shear-stress (θ) computed at gauge locations range from 0.0001 to 0.0003 at gauge 1, 0.01 to 0.03 at gauge 2, and 0.001 to 0.003 at gauge 3 (Figures S1, S2, and S3). From the map-based analysis, it is evident that the highest observed max. dimensionless bed shear-stresses are most pronounced along the shoreline and in the shallow water area of transition from the deeper to shallower water in the Lucerne Bay (Figure 11). The area with a max. dimensionless bed shear-stress $\theta \geq 0.3$ ranges from 0.2 to 0.6 x 10^6 m^2 for the various simulated bed-roughness coefficients (Table 4). See Supporting Information SI for the animation of the dimensionless bed shear-stress in the Lucerne Bay (Movie S2).

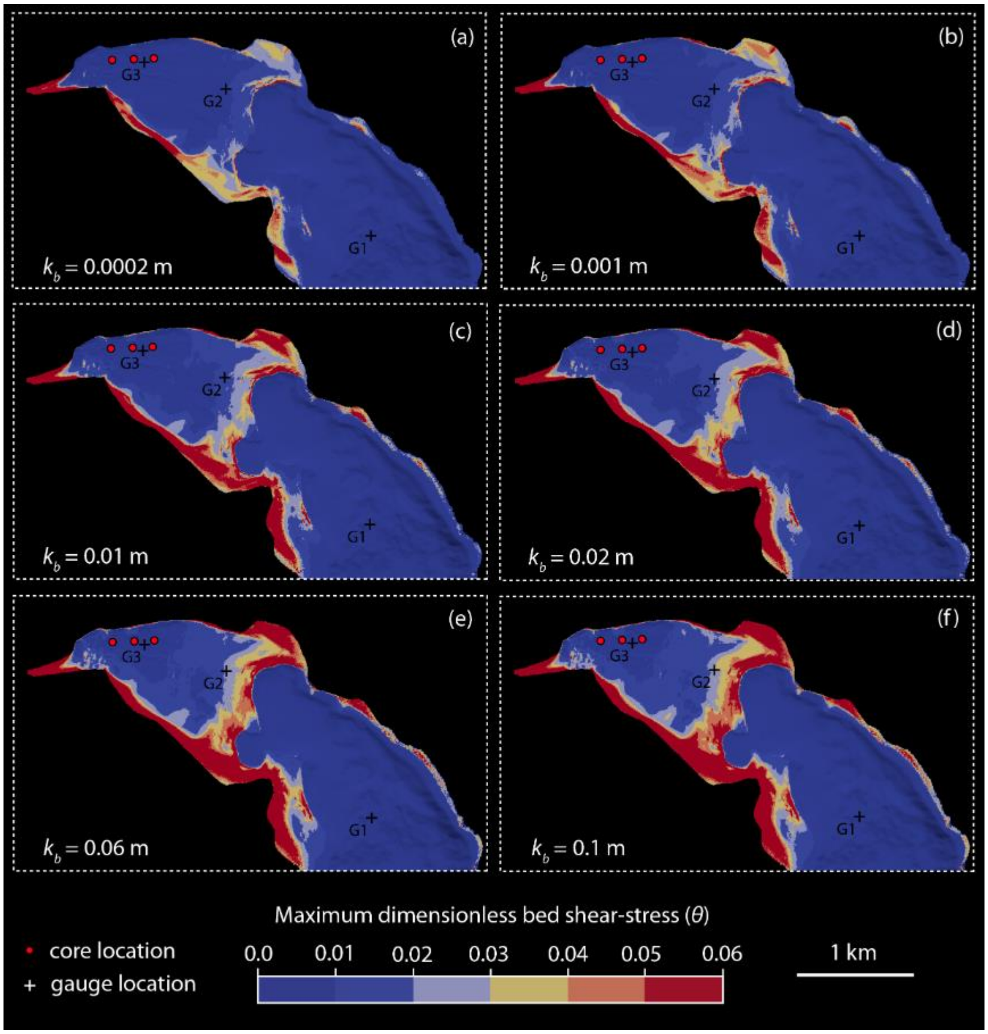

Figure 11. Results of the sensitivity analysis of bed roughness to the dimensionless bed shear-stress. The max. dimensionless bed shear-stress reached in each computational cell throughout the simulated time is shown for the simulation with different bed roughness (k_b: 0.0002–0.1 m). Sediment core (red dots) and gauge (black crosses) locations are shown on the map.

5 Discussion

5.1 Depositional History

5.1.1 Unit 4: Dense – Cohesive Silty Clay

The lowermost Unit 4, characterized as a dense, cohesive, light-gray clay to silt deposit has been previously described in other sediment cores in the area (Keller et al., 2020). These deposits are interpreted as glacio-lacustrine sediments deposited during an early lake phase around 15’000 yr. BP (Keller et al., 2020). The fine-grained cohesive sediment originates from the retreating Reuss Glacier and probably corresponds to rock flour delivered by glacial runoff. A gradual transition overlies Unit 4 discordant with a hiatus of several 1000 years. This hiatus is probably caused by the incision of the eroding outflowing Reuss River during lake-level low stands.

5.1.2 Unit 3: Light Brown Gyttja

With the construction of mills in the 13th century at the outflow of the lake, lake level was stabilized at today's level (Keller et al., 2020 and references therein). This early stabilized lake-level phase corresponds to the Unit 3, dated to 1174–1411 cal CE, which is characterized by organic-rich deposits with limited carbonate production and variable thickness along the coring transect (Figure 7).

5.1.2 Unit 2: Normal Graded Sand to Silt

The normally graded Unit 2 overlies Unit 3 with a sharp basal contact, indicating an abrupt deposition reflecting a severe event on Lake Lucerne. The narrow radiocarbon age range (1306–1437 cal CE) with minor age reversals as well as the normally graded sedimentary sequence of Unit 2 (Figure 5) indicate event deposition. Unit 2 is characterized by a fine sandy base and fines gradually upwards to a poorly sorted fine silt (Figures 5 and 6). A clear shift in the grain-size distribution is observable in Core LU18-2 at a depth of 95 and 60 cm (Figure 6). The two lowermost subunits have a well sorted grain-size distribution, whereas the two uppermost subunits are moderately to poorly sorted. Such types of normal grading haven been described for high-energy flows such as tsunamis and turbidity currents (Kuene & Menard, 1952; Middleton, 1967; Jaffe et al., 2011). The gradual upward decrease in grain size is a signature of deposition from suspension (Jaffe et al., 2012). This specific type of normal grading is termed suspension grading (Jaffe et al., 2012) and is primary caused by the settling velocity of the particles, but also by the flow velocity (Woodruff et al., 2008; Johnson et al., 2017). Thick normal graded deposits have been reported from the off- (e.g., Sakuna et al., 2012; Tamura et al., 2015) and onshore (e.g., Jaffe et al., 2012 and references therein) environment deposited by the inundation and backwash of marine tsunamis. For example, Kempf et al. (2015) have observed normal and multiple graded sand deposits with mud caps and variable thicknesses (5–60 cm) in two Chilean coastal lakes, that record the local inundation of the 1960 Great Chilean Earthquake tsunami. Of the few offshore tsunami deposits studied worldwide, several authors describe sharp lower and/or upper sedimentary contacts (e.g., van den Bergh et al., 2003; Sakuna et al., 2012; Abrantes et al., 2008; Goodman-Tchernov et al., 2009; Smedile et al., 2020) as observed at the basal contact of Unit 2. In Lake Sils, Nigg et al. (2021) observed thick normal graded sand deposits that were formed by the backwash currents of a prehistoric lake tsunami. Although the radiocarbon ages in Unit 2 are ~200 years younger than the historically described 1601 CE Lake Lucerne tsunami, the observed siliciclastic-rich, normally graded deposit (Unit 2) is interpreted to have been formed by this event. The single normally graded siliciclastic sand succession was deposited during a unique event. The sediment originates from the uppermost part of the lakebed in the Lucerne Bay, which was reworked by the erosive power of the wave, as is simulated in the numeric model and discussed in detail in Section 5.3 below. The event deposit was then formed at the depression by sediment deposition from suspension as the flow-velocity decreased. However, another historically reported tsunami event on Lake Lucerne in 1687 CE is unlikely to have the same order of magnitude in the Lucerne Bay because the tsunami was generated by a single subaqueous mass movement in a more distant basin and therefore no preserved sedimentary structures were observed in the sediment cores associated with this later event.

5.1.4 Unit 1: Carbonate Mud

Uppermost Unit 1 represents a modern lake system with high endogenous carbonate production in an oligotrophic lake (Bossard et al., 2001) that became more nutrient-rich during a period of eutrophication in the 1970s to 1980s (Theveneon et al., 2012). The high magnetic susceptibility is attributed to combustion particles associated with the development of steam navigation on Lake Lucerne from the beginning of the late 1830s.

5.2 Numerical Simulation

The selected tsunami generation mechanism, relying on the collapse of a selected area of the bathymetry is, despite its strongly simplified dynamics, in good agreement with similar, relying on more complex, approaches (Hilbe et al., 2015), reflecting a reasonable generated wave pattern. From both historical reports (e.g., the tsunami occurred in 1998 along the shores of the Sissano Lagoon in Papua New Guinea (Davies et al., 2003), it is well known that usually shorelines are hit by a wave train, with the first incoming wave characterized by a smaller amplitude with respect to the succeeding ones. Nevertheless, as also well described in (Lampela, 2019), near the shore the water most often undergoes a first drawback, forming a bore in a shallow area near the coast. This behavior is well reproduced by the numerical simulation obtained via BASEMENT. Indeed, considering for instance Figure 9, at 410 s, the water flows towards the center of the lake, i.e., creating a drawback (Figure 9a), while at 550 s one observes the formation of a bore in the shallow area, represented by the two distinct flow directions which meet to form a steep wave front, i.e., the bore (Figure 9b). Further, confirming the overall observations of tsunami behavior (e.g., Davies et al., 2003), the first simulated wave in the considered 1601 CE event results to be lower in height with respect to the subsequent ones, as can be seen for instance for the water-surface displacement over time in Figures S1, S2, and S3. The reported hydrodynamic quantities for the sensitivity analysis of the bed roughness height in the selected area of interest appear to not undergo significant changes where the water column is large (gauge 1). Indeed, as one may observe from Figures S1, S2, and S3, the wave amplitude and flow velocities appear less deformed in gauge 1, whereas in gauges 2 and 3 which are in shallow water, the wave amplitude displays several minor displacements when considering different k_b, as expected.

5.3 Sediment Erosion, Transport, and Deposition

5.3.1 Erosion, Maximum Dimensionless Bed Shear-Stress, and Bed Roughness

The max. dimensionless bed shear-stress is the key value that defines whether sediment is eroded by flow events (Van Rijn, 2007). The bed shear-stress reached during the propagation of the tsunami generated by the 1601 CE Weggis-slide (Figure 1) in the Lucerne Bay was numerically simulated with BASEMENT to better understand the erosion and mobilization potential of the tsunami waves. For this purpose, the influence of bed roughness on the incipient motion of particles was considered. Sediment may be eroded when the effective dimensionless bed shear-stress is larger than the dimensionless critical bed shear-stress, i.e., $\theta > \theta_{cr}$ (Choi &

Kwak, 2001). However, critical dimensionless bed shear-stress depends on the grain-size distribution and cohesion of the sediment bed (Houwing & Van Rijn, 1998). For the given situation, the threshold for incipient motion was chosen at $\theta = 0.03$, which has been previously suggested to be a reasonable number based on flume experiments (e.g., Shields, 1936; Houwing & Van Rijn, 1998). As soon as the threshold for incipient motion is reached, sediment particles may be entrained by the flow (van Rijn, 2007). Once sediment particles are set in motion, less energy is generally required to keep particles in motion after entrainment (Boggs, 2014).

The applied physical bed roughness (k_b) varies from 0.0002 to 0.1 m (Figure 11), which is a reasonable range from grain roughness to total physical bed roughness (Houwman & van Rijn, 1999). Total physical bed-roughness may be influenced by sedimentary bed forms (e.g., ripples and dunes), superimposed bed forms (e.g., megaripples), grain-size distribution and packing, mineralogical sediment composition, and the presence of an organic biofilm on the lakebed (van Rijn, 2007). Therefore, accurate estimates of total physical bed roughness are difficult to obtain. Houwman & van Rijn (1999), for example, have found that physical bed roughness of 0.1 m gives best agreement between measured and predicted current velocities in the North Sea at water depths of 5–10 m and a d_{50} of 200 μm. Thus, considering the above-mentioned factors and that surf beats are less expressed in the Lucerne Bay than at the North Sea coast, physical bed roughness of 0.02 to 0.06 m is a reasonable and realistic value for the given situation.

Considering the above limitations in the estimation of incipient motion, our simulation shows large areas with a dimensionless bed shear-stress $\theta \geq 0.03$ (Figure 11), indicating large amounts of sediment may have been eroded, transported, and resuspended by the main wave pulses of the 1601 CE tsunami in the Lucerne Bay. The areal extent of max. dimensionless bed shear-stress $\theta \geq 0.03$ computed for different physical bed-roughness is in the order of 0.2–0.6 x 10^6 m^2 and follows the regression curve $y = 0.8225\ k_b^{0.163}$ (Figure 12a). A simple estimate of the erosion volume (4 to 11.5 x 10^4 m^3; Figure 12b) can be calculated based on a homogeneous thickness of erosion (0.02–0.2 m) on the area with $\theta \geq 0.03$ (Table S6). Thus, our simulations show clearly that substantial amount of sediment gets eroded and mobilized by the waves. The erosion mostly affects the uppermost water-rich layer near the lakebed. The age data of Unit 2 (1306 to 1442 cal CE; Table 3) with radiocarbon ages of up to 200 years older than the tsunami event confirms that sediment may get mobilized to a chronostratigraphic depth of 200 years, corresponding to a thickness of up to 20 cm at a sedimentation rate of 0.1 cm yr^{-1}. Therefore, eroded volume in the Lucerne Bay is likely in the order of 10^4 to 10^5 m^3 (Figure 12b; k_b: 0.02–0.06 m) with an erosional thickness of 0.2 m.

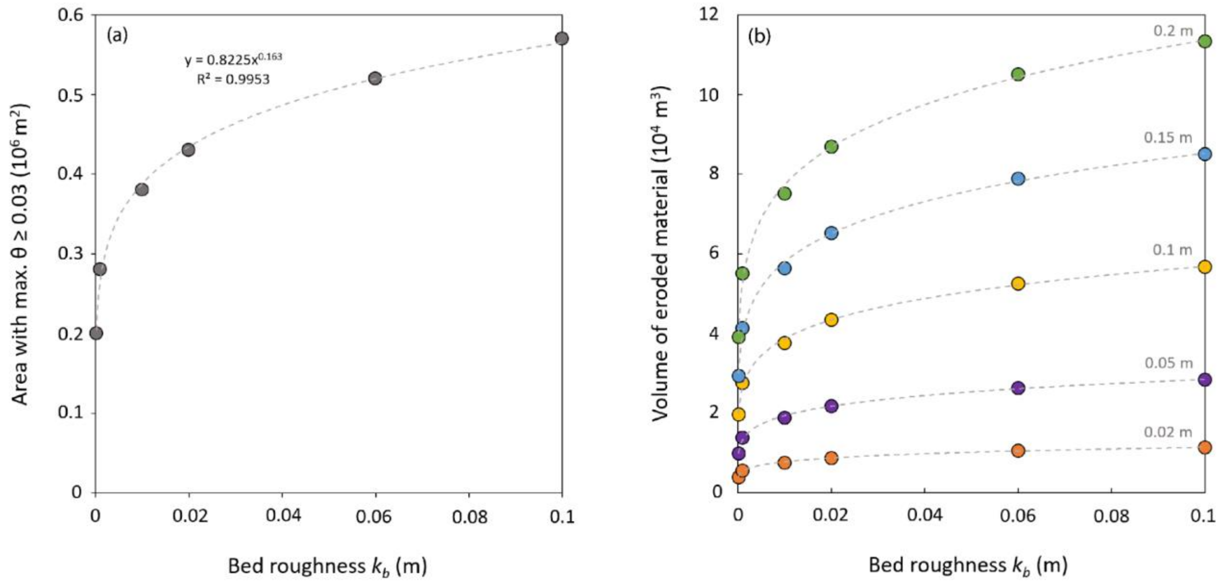

Figure 12: (a) Mapped area with a max. dimensionless bed shear-stress $\theta \geq 0.03$ reached computed with different bed roughness k_b. (b) Estimation of remobilized sediment volumes with different homogeneous erosional thicknesses and bed roughness k_b.

5.3.2 Sediment Source

The numerical simulations clearly show where and when the tsunami wave causes bed shear-stress in the Lucerne Bay capable of substantial sediment erosion and mobilization (Figure 12). Erosional forces are pronounced in the shallow-water area of geomorphological obstacles marking the transition from the deeper to the shallower area of the Lucerne Bay and along the lakeshore, as indicated by the computed max. dimensionless bed shear-stress (Figure 11). These areas are likely the sediment source of remobilized sediment particles during the 1601 CE tsunami inundation of the Lucerne Bay. Another important sediment source is the lakeshore, where predominantly siliciclastic sand is found (e.g., lake-surface sediment Sample LS-3). At these locations, constant wave motion leads to sandy-dominated surface sediments from winnowing of fines.

5.3.3 Sediment Transport and Deposition

The sediment transport towards the coring site can be observed by visualizing vectors of flow-velocity magnitude indicating the sediment transport direction (Figure 9). Three main wave pulses propagate in the Lucerne Bay in the first 1800 s after the instantaneous simulated Weggis-slide collapse (Figure 10). During the first wave, a strong surge towards the wave trough is observable (Figure 9a). At this stage, sediment particles may be mobilized and brought into suspension. With the arrival of the 2^{nd} wave expressed as an impressive bore-like wave, particles are then transported westwards towards the coring location (Figure 9d). These main wave pulses have high flow velocities (> 2 m s^{-1}; Figure 10b) and specific discharges (> 4 m^3 s^{-1}; Figures S1, S2, and S3) that are capable to transport large amounts of sediment from the areas with high bed shear-stress towards the coring location. At the coring location, due to the geomorphological depression, flow velocity drops instantaneously, and sediments are deposited from suspension forming the graded event deposit.

A depositional volume of 2×10^4 m^3 is estimated from the thickness of Unit 2 in recovered sediment cores and multibeam bathymetry map (Figure 2b). This estimate fits well with the proposed eroded sediment volume in the order of 10^4 to10^5 m^3, that is estimated with the numerical model more accurate estimation of eroded volume would be possible by using a fully featured model for suspended-sediment transport, which is currently still under development. Such a model would allow for simulation of variable erosion related to the dimensionless bed shear-stress and provide more realistic transport of the sediment with the flow. However, many uncertainties may persist, e.g., sediment-erosion thickness is likely not homogenous over the area and sediment erosion may be strongly influenced by local variations of sediment composition (e.g., mineralogy, grain-size distribution, and bed roughness). However, the presented methodology proves to be a reasonable simplification of the complex mechanism of erosion by tsunami waves and allows for basic reconstruction of related events and processes involved.

6 Conclusions

An offshore event deposit was observed in sediment cores recovered along a transect across a depression in the shallow-subaqueous environment of Lucerne Bay. The normally graded deposit with a thickness of up to 60 cm consists predominantly of siliciclastic sand- to silt-sized particles with increased amounts of coarse sand-sized carbonate shell fragments at the base. The deposit has a sharp basal contact with horizontally bedded organic, mostly woody particles that become more abundant in the upper part of the deposit. Radiocarbon dates of terrestrial plant macro remains isolated from the clastic deposit yield ages in the range of 1306-1442 cal CE.

The sedimentary features clearly reflect deposition from a high-flow event, which we interpret to be the historically reported 1601 CE Lake Lucerne tsunami. This interpretation is supported by i) the grain-size pattern of Unit 2 indicating suspension settling, ii) the narrow 200 years age offset of the event deposit indicating erosion, mobilization of the uppermost sediment column, as well as iii) the performed numerical tsunami-wave propagation and bed shear-stress simulation in the Lucerne Bay, providing a criterion for incipient motion of sediment by the incoming waves.

The numerical simulation of the 1601 CE Lake Lucerne tsunami was simulated using the software BASEMENT by an instantaneous collapse of the second largest subaqueous mass-movement failed during the 1601 CE earthquake. In addition to simulating the wave propagation, water surface-displacement, and flow-velocity magnitude, the dimensionless bed shear-stress was used to characterize and locate areas of tsunami-induced sediment erosion in the shallow-subaqueous environment of Lucerne Bay. The simulated results clearly show that the critical dimensionless bed shear-stress is exceeded in large areas where significant erosion must have occurred. Flow direction pointing from the erosional areas toward the sediment sink in the depression indicate sediment transport towards the coring locations.

Our study thus documents the high potential of combining sedimentological observations of event deposits with numerical simulations of water motion. This approach is not restricted to lacustrine systems and mass movement-induced tsunami waves but can be applied to any basin where high-flow events occur.

Acknowledgments

This study is funded by the Swiss National Science Foundation (research grant no.: 171017) and is embedded in the SNSF Sinergia Project “Lake tsunami: causes, controls and hazard”. We acknowledge Nicole Schwendener and the Institute of Anatomy, University of Bern for their support with CT scanning, Daniela Fischer and the Institute of Geography, University of Bern for their support with the grain-size determination. Sönke Szidat and the Department of Chemistry and Biochemistry, University of Bern are acknowledged for the radiocarbon dating. Julijana Krbanjevic is acknowledged for her help with the geochemical analysis. Firtz Schlunegger and Beat Keller are thanked for their useful comments on the manuscript. Franzyska Nyffenegger, Dominik Amschwand, Julijana Krbanjevic, Flavio Huber, Evelyne Margelisch, Michael Strupler, Stefano Fabbri, Adrian Gilli, and Marina Morlock are acknowledged for their support during the coring campaign. Nikola Janevski is acknowledged for his help in collecting lake-surface samples from a sailboat.

Data Availabitliy Statement

Data of core scans (MSCL and XRF), LDA particle-size measurements, virtual gauge used for the sensitivity analysis, interpolated lake bathymetry of the area used for numerical wave-propagation simulation, and coordinates of sediment cores, lake-surface samples, and virtual gauges used in this research are submitted to the data repository Pangaea and will be freely accessible under the CC-BY license after publication. The BASEMENT software used in this research is described in detail in Vetsch et al. (2020).

References

Abrantes, F., Alt-Epping, U., Lebreiro, S., Voelker, A., & Schneider, R. (2008). Sedimentological record of tsunamis on shallow-shelf areas: The case of the 1969 AD and 1755 AD tsunamis on the Portuguese Shelf off Lisbon. *Marine Geology, 249*(3-4), 283-293. doi.org/10.1016/j.margeo.2007.12.004

Apotsos, A., Gelfenbaum, G., Jaffe, B., Watt, S., Peck, B., Buckley, M., & Stevens, A. (2011). Tsunami inundation and sediment transport in a sediment-limited embayment on American Samoa. *Earth-Science Reviews, 107*(1-2), 1-1. doi.org/10.1016/j.earscirev.2010.11.001

Apotsos, A., Gelfenbaum, G., & Jaffe, B. (2012). Time-dependent onshore tsunami response. *Coastal Engineering, 64*, 73-86. doi.org/10.1016/j.coastaleng.2012.01.001

BAFU (Ed.) (2009). Hydrologisches Jahrbuch der Schweiz 2008. *Umwelt-Wissen Nr. 0921*, Swiss Federal Office for the Environment, Bern, 578 pp.

Billeter, J. (1923). Pfarrer Jakob Billeter von Aegeri und seine Chronik. *Heimat-Klänge, Sonntags-Beilage zu den «Zuger Nachrichten»*, 3. Jahrgang, Nr. 4, 28. January, 15-16.

Bobrowsky, P. T., & Marker, B. (Eds.) (2018). *Encyclopedia of Engineering Geology*. Cham: Springer. doi.org/10.1007/978-3-319-73568-9

Boggs Jr, S. (2014). Principles of Sedimentology and Stratigraphy, Fifth Edition. Pearson, Harlow, pp. 564.

Bossard, P., Gammeter, S., Lehmann, C., Schanz, F., Bachofen, R., Bürgi, H. R., et al. (2001). Limnological description of the lakes Zürich, Lucerne, and Cadagno. *Aquatic Sciences, 63*(3), 225-249. doi.org/10.1007/PL00001353

Buffington, J. M., & Montgomery, D. R. (1997). A systematic analysis of eight decades of incipient motion studies, with special reference to gravel-bedded rivers. *Water Resources Research, 33*(8), 1993-2029. doi.org/10.1029/96WR03190

Bünti, J.L. (1973). Chronik des Johann Laurentz Bünti, Landammann, 1661-1736. *Beiträge zur Geschichte Nidwaldens, 34*,26-27.

Choi, S. U., & Kwak, S. (2001). Theoretical and probabilistic analyses of incipient motion of sediment particles. *KSCE Journal of Civil Engineering, 5*(1), 59-65. doi.org/10.1007/BF02830727

Costa, P. J., & Andrade, C. (2020). Tsunami deposits: Present knowledge and future challenges. *Sedimentology*, *67*(3), 1189-1206. doi.org/10.1111/sed.12724

Cysat, R. (1969). Collectanea Chronica und denkwürdige Sachen pro Chronica Lucernensi et Helvetiae. *Erster Band, zweiter Teil* (Eds J. Schmid and D. Schilling), pp. 879-888. Diebold Schilling Verlag, Luzern.

Davies, H. L., Davies, J. M., Perembo, R. C. B., & Lus, W. Y. (2003). The Aitape 1998 tsunami: Reconstructing the event from interviews and field mapping. *Pure and Applied Geophysics, 160*(10-11), 1895-1922. doi.org/10.1007/s00024-003-2413-1

Dawson, A. G., & Stewart, I. (2008). Offshore tractive current deposition: the forgotten tsunami sedimentation process. In *Tsunamiites* (pp. 153-161). Elsevier. doi.org/10.1016/B978-0-444-51552-0.00010-2

Dietrich, J. (1689). Diarium von P. Josef Dietrich von Einsiedeln (1645-1704), Bd. 6. *Klosterarchiv Einsiedeln, KAE A.HB.6*, pp. 202.

Einsele, G., Chough, S. K., & Shiki, T. (1996). Depositional events and their records-an introduction. *Sedimentary Geology, 104*(1-4), 1-9. doi.org/10.1016/0037-0738(95)00117-4

Fäh, D., Giardini, D., Kästli, P., Deichmann, N., Gisler, M., Schwarz-Zanetti, G., et al. (2011). *ECOS-09 Earthquake Catalogue of Switzerland, Release 2011, Report SED/ECOS/R/001/20110417*. Swiss Seismological Service, ETH Zürich, 42 pp.

Favrod, J (1991). La Chronique de Marius d'Avenches (455-581): Texte, Traduction et Commentaire (Vol. 4). Section d'histoire, Faculté des lettres, Université de Lausanne.

Feldens, P., Schwarzer, K., Szczucinski, W., Stattegger, K., Sakuna, D., & Somgpongchaiykul, P. (2009). Impact of 2004 Tsunami on Seafloor Morphology and Offshore Sediments, Pakarang Cape, Thailand. *Polish Journal of Environmental Studies, 18*(1).

Fujiwara, O. (2008). Bedforms and sedimentary structures characterizing tsunami deposits. In *Tsunamiites* (pp. 51-62). Elsevier. doi.org/10.1016/B978-0-444-51552-0.00004-7

Funk, H., Buxtorf, A., Christ, P., Egli, D., Estoppey, D., Gebel, Ch., et al. (2013). Geologischer Atlas der Schweiz, Blatt 1170, Alpnach (Nr. 137). *Schweizerische Geologische Kommission*, scale 1:25 000, 1 sheet.

Fritz, H. M., Kalligeris, N., Borrero, J. C., Broncano, P., & Ortega, E. (2008). The 15 August 2007 Peru tsunami runup observations and modeling. *Geophysical Research Letters, 35*(10). doi.org/10.1029/2008GL033494

Gardner, J. V., Mayer, L. A., & Hughs Clarke, J. E. (2000). Morphology and processes in lake Tahoe (California-Nevada). *Geological Society of America Bulletin, 112(*5), 736-746. doi.org/10.1130/0016-7606(2000)112<736:MAPILT>2.0.CO;2

Goodman-Tchernov, B. N., & Austin Jr, J. A. (2015). Deterioration of Israel's Caesarea Maritima's ancient harbor linked to repeated tsunami events identified in geophysical mapping of offshore stratigraphy. *Journal of Archaeological Science: Reports, 3*, 444-454. doi.org/10.1016/j.jasrep.2015.06.032

Goodman-Tchernov, B. N., Dey, H. W., Reinhardt, E. G., McCoy, F., & Mart, Y. (2009). Tsunami waves generated by the Santorini eruption reached Eastern Mediterranean shores. *Geology, 37*(10), 943-946. doi.org/10.1130/G25704A.1

Goto, K., Chagué-Goff, C., Fujino, S., Goff, J., Jaffe, B., Nishimura, Y., et al. (2011a). New insights of tsunami hazard from the 2011 Tohoku-oki event. *Marine Geology, 290*(1-4), 46-50. doi.org/10.1016/j.margeo.2011.10.004

Goto, K., Ikehara, K., Goff, J., Chagué-Goff, C., & Jaffe, B. (2014). The 2011 Tohoku-oki tsunami-Three years on. *Marine Geology, 358*, 2-11. doi.org/10.1016/j.margeo.2014.08.008

Goto, K., Takahashi, J., Oie, T., & Imamura, F. (2011b). Remarkable bathymetric change in the nearshore zone by the 2004 Indian Ocean tsunami: Kirinda Harbor, Sri Lanka. *Geomorphology, 127*(1-2), 107-116. doi.org/10.1016/j.geomorph.2010.12.011

Hantke, R., Bollinger, D., & Kopp, J. (2005). Geologischer Atlas der Schweiz, Blatt 1151, Rigi (Nr. 116). *Schweizerische Geologische Kommission*, scale 1:25 000, 1 sheet.

Haraguchi, T., Goto, K., Sato, M., Yoshinaga, Y., Yamaguchi, N., & Takahashi, T. (2013). Large bedform generated by the 2011 Tohoku-oki tsunami at Kesennuma Bay, Japan. *Marine Geology, 335*, 200-205. doi.org/10.1016/j.margeo.2012.11.005

Heidarzadeh, M., Muhari, A., & Wijanarto, A. B. (2019). Insights on the source of the 28 September 2018 Sulawesi tsunami, Indonesia based on spectral analyses and numerical simulations. *Pure and Applied Geophysics, 176*(1), 25-43. doi.org/10.1007/s00024-018-2065-9

Hilbe, M., & Anselmetti, F. S. (2014). Signatures of slope failures and river-delta collapses in a perialpine lake (Lake Lucerne, Switzerland). *Sedimentology, 61*(7), 1883-1907. doi.org/10.1111/sed.12120

Hilbe, M., & Anselmetti, F. S. (2015). Mass movement-induced tsunami hazard on perialpine Lake Lucerne (Switzerland): scenarios and numerical experiments. *Pure and Applied Geophysics, 172*(2), 545-568. doi.org/10.1007/s00024-014-0907-7

Hilbe, M., Anselmetti, F.S., Eilertsen, R.S., Hansen, L. & Wildi, W. (2011). Subaqueous morphology of Lake Lucerne (Central Switzerland): implications for mass movements and glacial history. *Swiss Journal of Geosciences, 104*(3), 425-433. doi.org/10.1007/s00015-011-0083-z

Houwman, K. T., & Van Rijn, L. C. (1999). Flow resistance in the coastal zone. *Coastal Engineering, 38(*4), 261-273. doi.org/10.1016/S0378-3839(99)00049-6

Huntington, K., Bourgeois, J., Gelfenbaum, G., Lynett, P., Jaffe, B., Yeh, H., & Weiss, R. (2007). Sandy signs of a tsunami's onshore depth and speed. *Eos, Transactions American Geophysical Union, 88(*52), 577-578. doi.org/10.1029/2007EO520001

Ikehara, K., Irino, T., Usami, K., Jenkins, R., Omura, A., & Ashi, J. (2014). Possible submarine tsunami deposits on the outer shelf of Sendai Bay, Japan resulting from the 2011 earthquake and tsunami off the Pacific coast of Tohoku. *Marine Geology, 358*, 120-127. doi.org/10.1016/j.margeo.2014.11.004

Jaffe, B. E., & Gelfenbuam, G. (2007). A simple model for calculating tsunami flow speed from tsunami deposits. *Sedimentary Geology, 200*(3-4), 347-361. doi.org/10.1016/j.sedgeo.2007.01.013

Jaffe, B.E., Buckley, M., Richmond, B., Strotz, L., Etienne, S., Clark, K., et al. (2011). Flow speed estimated by inverse modeling of sandy sediment deposited by the 29 September 2009 tsunami near Satitoa, east Upolu, Samoa. *Earth-Science Reviews, 107*(1-2), 23-37. doi.org/10.1016/j.earscirev.2011.03.009

Jaffe, B. E., Goto, K., Sugawara, D., Richmond, B. M., Fujino, S., & Nishimura, Y. (2012). Flow speed estimated by inverse modeling of sandy tsunami deposits: results from the 11 March 2011 tsunami on the coastal plain near the Sendai Airport, Honshu, Japan. *Sedimentary Geology, 282*, 90-109. doi.org/10.1016/j.sedgeo.2012.09.002

Johnson, J. P., Delbecq, K., & Kim, W. (2017). Predicting paleohydraulics from storm surge and tsunami deposits: Using experiments to improve inverse model accuracy. *Journal of Geophysical Research: Earth Surface, 122*(4), 760-781. doi.org/10.1002/2015JF003816

Keller, B. (2013). Geologische Geschichte der Luzerner Reuss. In *Gestautes Wasser - Regulierter See: Geschichte, Bau und Betrieb der Reusswehranlage in Luzern* (pp. 105-123). Lehrmittelverlag Kanton Luzern.

Keller, B. (2017). Massive rock slope failure in Central Switzerland: history, geologic-geomorphological predisposition, types and triggers, and resulting risks. *Landslides, 14*(5), 1633-1653. doi.org/10.1007/s10346-017-0803-1

Keller, B. (2020). Lake Lucerne and Its Spectacular Landscape. In *Landscapes and Landforms of Switzerland* (pp. 305-323). Springer, Cham. doi.org/10.1007/978-3-030-43203-4_21

Kopp, J., Bendel, L., & Buxtorf, A., (1955). Geologischer Atlas der Schweiz, Blatt 1150, Luzern (Nr. 28). *Schweizerische Geologische Kommission*, scale 1:25 000, 1 sheet.

Kempf, P., Moernaut, J., Van Daele, M., Vermassen, F., Vandoorne, W., Pino, M., ... & De Batist, M. (2015). The sedimentary record of the 1960 tsunami in two coastal lakes on Isla de Chiloé, south central Chile. *Sedimentary geology, 328*, 73-86. doi.org/10.1016/j.sedgeo.2015.08.004

Kihara, N., Fujii, N., & Matsuyama, M. (2012). Three-dimensional sediment transport processes on tsunami-induced topography changes in a harbor. *Earth, planets and space, 64*(10), 787-797. doi.org/10.5047/eps.2011.05.036

Kremer, K., Anselmetti, F. S., Evers, F. M., Goff, J., & Nigg, V. (2020) Freshwater (paleo) tsunamis-a review. *Earth-science reviews*, 103447. doi.org/10.1016/j.earscirev.2020.103447

Kremer, K., Hilbe, M., Simpson, G., Decrouy, L., Wildi, W., & Girardclos, S. (2015). Reconstructing 4000 years of mass movement and tsunami history in a deep peri-Alpine lake (Lake Geneva, France-Switzerland). *Sedimentology, 62*(5), 1305-1327. doi.org/10.1111/sed.12190

Kremer, K., Marillier, F., Hilbe, M., Simpson, G., Dupuy, D., Yrro, B. J., et al. (2014). Lake dwellers occupation gap in Lake Geneva (France-Switzerland) possibly explained by an earthquake-mass movement-tsunami event during Early Bronze Age. *Earth and Planetary Science Letters, 385*, 28-39. doi.org/10.1016/j.epsl.2013.09.017

Kremer, K., Simpson, G., & Girardclos, S. (2012). Giant Lake Geneva tsunami in ad 563. *Nature Geoscience, 5*(11), 756-757. doi.org/10.1038/ngeo1618

Klyuchevskii, A. V., Demyanovich, V. M., & Klyuchevskaya, A. A. (2012). The possibility of a tsunami on Lake Baikal. In *Doklady Earth Sciences* (Vol. 442, No. 1, pp. 130-134). SP MAIK Nauka/Interperiodica. doi.org/10.1134/S1028334X1201014X

Kuenen, P. H., & Menard, H. W. (1952). Turbidity currents, graded and non-graded deposits. Journal of Sedimentary Research, 22(2), 83-96. doi.org/10.1306/D42694CC-2B26-11D7-8648000102C1865D

Kuriyama, Y., Chida, Y., Uno, Y., & Honda, K. (2020). Numerical simulation of sedimentation and erosion caused by the 2011 Tohoku Tsunami in Oarai Port, Japan. *Marine Geology, 427*, 106225. doi.org/10.1016/j.margeo.2020.106225

Lampela, K.M. (2019). Tsunami shoaling theory. *Computational Methods and Experimental Measurements XIX & Earthquake Resistant Engineering Structures XII*. doi.org/10.2495/ERES190101

Lee, H., & Balachandar, S. (2012). Critical shear stress for incipient motion of a particle on a rough bed. *Journal of Geophysical Research: Earth Surface, 117*(F1). doi.org/10.1029/2011JF002208

Mantz, P. A. (1977). Incipient transport of fine grains and flakes by fluids-extended shield diagram. ASCE. *Journal of the Hydraulics division, 103*. doi.org/10.1061/JYCEAJ.0004766

Michel, C., Bleicher, N., Brombacher, C., Hüster Plogmann, H., Ismail-Meyer, K., & Rehazek, A. (2012). Pfahlbauten am Vierwaldstättersee-der steinzeitliche Siedlungsplatz in Kehrsiten. *Archäologie der Schweiz, 35*(2), 56-71.

Middleton, G. V. (1967). Experiments on density and turbidity currents: III. Deposition of sediment. Canadian Journal of Earth Sciences, 4(3), 475-505. doi.org/10.1139/e67-025

Montandon, F. (1925). Les Eboulements de la Dent du Midi et du Grammont (Examen critique de la Question du Tauredunum). *Le Globe. Revue genevoise de géographie, 64*(1), 35-91. doi.org/10.3406/globe.1925.2349

Moore, J. G., Schweickert, R. A., Robinson, J. E., Lahren, M. M., & Kitts, C. A. (2006). Tsunami-generated boulder ridges in Lake Tahoe, California-Nevada. *Geology, 34*(11), 965-968. doi.org/10.1130/G22643A.1

Mountjoy, J. J., Wang, X., Woelz, S., Fitzsimons, S., Howarth, J. D., Orpin, A. R., & Power, W. (2019). Tsunami hazard from lacustrine mass wasting in Lake Tekapo, New Zealand. *Geological Society, London, Special Publications, 477*(1), 413-426. doi.org/10.1144/SP477.21

Noda, A., Katayama, H., Sagayama, T., Suga, K., Uchida, Y., Satake, K., et al. (2007). Evaluation of tsunami impacts on shallow marine sediments: An example from the tsunami caused by the 2003 Tokachi-oki earthquake, northern Japan. *Sedimentary Geology, 200*(3-4), 314-327. doi.org/10.1016/j.sedgeo.2007.01.010

Nigg, V., Wohlwend, S., Hilbe, M., Bellwald, B., Fabbri, S. C., de Souza, G. F., et al. (2021). A tsunamigenic delta collapse and its associated tsunami deposits in and around Lake Sils, Switzerland. *Natural Hazards*, 1-35. doi.org/10.1007/s11069-021-04533-y

Ontowirjo, B., Paris, R., & Mano, A. (2013). Modeling of coastal erosion and sediment deposition during the 2004 Indian Ocean tsunami in Lhok Nga, Sumatra, Indonesia. *Natural hazards, 65*(3), 1967-1979. doi.org/10.1007/s11069-012-0455-3

Paris, R., Fournier, J., Poizot, E., Etienne, S., Morin, J., Lavigne, F., & Wassmer, P. (2010). Boulder and fine sediment transport and deposition by the 2004 tsunami in Lhok Nga (western Banda Aceh, Sumatra, Indonesia): a coupled offshore-onshore model. *Marine Geology, 268*(1-4), 43-54. doi.org/10.1016/j.margeo.2009.10.011

Pritchard, D., & Dickinson, L. (2008). Modelling the sedimentary signature of long waves on coasts: implications for tsunami reconstruction. *Sedimentary Geology, 206*(1-4), 42-57. doi.org/10.1016/j.sedgeo.2008.03.004

Ramsey, C. B. (2009). Bayesian analysis of radiocarbon dates. *Radiocarbon, 51*(1), 337-360. doi.org/10.1017/S0033822200033865

Reimer, P. J., Austin, W. E., Bard, E., Bayliss, A., Blackwell, P. G., Ramsey, C. B., et al. (2020). The IntCal20 northern hemisphere radiocarbon age calibration curve (0-55 cal kBP). *Radiocarbon, 62*(4), 725-757. doi.org/10.1017/RDC.2020.41

Riou, B., Chaumillon, E., Schneider, J. L., Corrège, T., & Chagué, C. (2020). The sediment-fill of Pago Pago Bay (Tutuila Island, American Samoa): New insights on the sediment record of past tsunamis. *Sedimentology, 67*(3), 1577-1600. doi.org/10.1111/sed.12574

Roberts, N. J., McKillop, R. J., Lawrence, M. S., Psutka, J. F., Clague, J. J., Brideau, M. A., & Ward, B. C. (2013). Impacts of the 2007 landslide-generated tsunami in Chehalis Lake, Canada. In *Landslide science and practice* (pp. 133-140). Springer, Berlin, Heidelberg. doi.org/10.1007/978-3-642-31319-6_19

Sakuna, D., Szczuciński, W., Feldens, P., Schwarzer, K., & Khokiattiwong, S. (2012). Sedimentary deposits left by the 2004 Indian Ocean tsunami on the inner continental shelf offshore of Khao Lak, Andaman Sea (Thailand). *Earth, planets and space, 64*(10), 11. doi.org/10.5047/eps.2011.08.010

Schlunegger, F., Matter, A., Burbank, D. W., & Klaper, E. M. (1997). Magnetostratigraphic constraints on relationships between evolution of the central Swiss Molasse basin and Alpine orogenic events. *Geological Society of America Bulletin, 109*(2), 225-241. doi.org/10.1130/0016-7606(1997)109<0225:MCORBE>2.3.CO;2

Schnellmann, M., Anselmetti, F. S., Giardini, D., & McKenzie, J. A. (2005). Mass movement-induced fold-and-thrust belt structures in unconsolidated sediments in Lake Lucerne (Switzerland). *Sedimentology, 52*(2), 271-289. doi.org/10.1111/j.1365-3091.2004.00694.x

Schnellmann, M., Anselmetti, F.S., Giardini, D., & McKenzie, J. A. (2006). 15,000 Years of mass-movement history in Lake Lucerne: implications for seismic and tsunami hazards. *Eclogae Geologicae Helveticae, 99*(3), 409-428. doi.org/10.1007/s00015-006-1196-7

Schnellmann, M., Anselmetti, F. S., Giardini, D., McKenzie, J. A., & Ward, S. (2002). Prehistoric earthquake history revealed by lacustrine slump deposits. *Geology, 30*(12), 1131-1134. doi.org/10.1130/0091-7613(2002)030<1131:PEHRBL>2.0.CO;2

Schwarz-Zanetti, G., Deichmann, N., Fäh, D., Giardini, D., Jimenez, M.-J., Masciadri, V., et al. (2003). The earthquake in Unterwalden on September 18, 1601: a historico-critical macroseismic evaluation. *Eclogae Geologicae Helveticae, 96*(3), 441-450.

Shields, A. (1936). Anwendung der Aehnlichkeitsmechanik und der Turbulenzforschung auf die Geschiebebewegung. PhD Thesis Technical University Berlin.

Siegenthaler, C., Finger, W., Kelts, K. &Wang, S. (1987). Earthquake and seiche deposits in Lake Lucerne, Switzerland. *Eclogae Geologicae Helvetiae, 80*(1), 241-260.

Smedile, A., De Martini, P. M., Pantosti, D., Bellucci, L., Del Carlo, P., Gasperini, L., et al. (2011). Possible tsunami signatures from an integrated study in the Augusta Bay offshore (Eastern Sicily-Italy). *Marine Geology, 281*(1-4), 1-13. doi.org/10.1016/j.margeo.2011.01.002

Smedile, A., Molisso, F., Chagué, C., Iorio, M., De Martini, P. M., Pinzi, S., et al. (2020). New coring study in Augusta Bay expands understanding of offshore tsunami deposits (Eastern Sicily, Italy). *Sedimentology, 67*(3), 1553-1576. doi.org/10.1111/sed.12581

Spiske, M., Piepenbreier, J., Benavente, C., & Bahlburg, H. (2013). Preservation potential of tsunami deposits on arid siliciclastic coasts. *Earth-Science Reviews, 126*, 58-73. doi.org/10.1016/j.earscirev.2013.07.009

Spiske, M., Weiss, R., Bahlburg, H., Roskosch, J., & Amijaya, H. (2010). The TsuSedMod inversion model applied to the deposits of the 2004 Sumatra and 2006 Java tsunami and implications for estimating flow parameters of palaeo-tsunami. *Sedimentary Geology, 224*(1-4), 29-37. doi.org/10.1016/j.sedgeo.2009.12.005

Strupler, M., Bacigaluppi, P., Kremer, K., Vetsch, D., Anselmetti, F., Boes, R., & Wiemer, S. (2020). Abschätzung der Gefährdung durch Tsunamis in perialpinen Seen infolge Unterwasserhangrutschungen. *Wasser Energie Luft, 112*(1), 11-16.

Strupler, M., Danciu, L., Hilbe, M., Kremer, K., Anselmetti, F. S., Strasser, M., & Wiemer, S. (2018a). A subaqueous hazard map for earthquake-triggered landslides in Lake Zurich, Switzerland. *Natural Hazards, 90*(1), 51-78. doi.org/10.1007/s11069-017-3032-y

Strupler, M., Hilbe, M., Kremer, K., Danciu, L., Anselmetti, F.S., Strasser, M. & Wiemer, S. (2018b). Subaqueous landslide-triggered tsunami hazard for Lake Zurich, Switzerland. *Swiss Journal of Geosciences, 111*(1), 353-371. doi.org/10.1007/s00015-018-0308-5

Stuiver, M., & Polach, H. A. (1977) Discussion reporting of 14 C data. *Radiocarbon, 19*(3), 355-363. doi.org/10.1017/S0033822200003672

Sugawara, D., Minoura, K., Nemoto, N., Tsukawaki, S., Goto, K., & Imamura, F. (2009). Foraminiferal evidence of submarine sediment transport and deposition by backwash during the 2004 Indian Ocean tsunami. *Island Arc, 18*(3), 513-525. doi.org/10.1111/j.1440-1738.2009.00677.x

Suzuki, W., Aoi, S., Sekiguchi, H., & Kunugi, T. (2011). Rupture process of the 2011 Tohoku-Oki mega-thrust earthquake (M9. 0) inverted from strong-motion data. *Geophysical Research Letters, 38*(7). doi.org/10.1029/2011GL049136

Tamura, T., Sawai, Y., Ikehara, K., Nakashima, R., Hara, J., & Kanai, Y. (2015). Shallow-marine deposits associated with the 2011 Tohoku-oki tsunami in Sendai Bay, Japan. *Journal of Quaternary Science, 30*(4), 293-297. doi.org/10.1002/jqs.2786

Tang, H., & Weiss, R. (2015). A model for tsunami flow inversion from deposits (TSUFLIND). *Marine geology, 370*, 55-62. doi.org/10.1016/j.margeo.2015.10.011

Thevenon, F., Adatte, T., Poté, J., & Spangenberg, J. E. (2012). Recent human-induced trophic change in the large and deep perialpine Lake Lucerne (Switzerland) compared to historical geochemical variations. *Palaeogeography, Palaeoclimatology, Palaeoecology, 363*, 37-47. doi.org/10.1016/j.palaeo.2012.08.010

Vanzo, D., Peter, S., Vonwiller, L., Buergler, M., Weberndorfer, M., Siviglia, A., et al. (subm.). BASEMENT v3: a modular freeware fro river process modelling over multiple computational backends. *Environmental Modelling & Software*. https://arxiv.org/abs/2102.12862

Van den Bergh, G. D., Boer, W., De Haas, H., Van Weering, T. C., & Van Wijhe, R. (2003). Shallow marine tsunami deposits in Teluk Banten (NW Java, Indonesia), generated by the 1883 Krakatau eruption. *Marine Geology, 197*(1-4), 13-34. doi.org/10.1016/S0025-3227(03)00088-4

Van Rijn, L. C. (2007). Unified view of sediment transport by currents and waves. I: Initiation of motion, bed roughness, and bed-load transport. *Journal of Hydraulic engineering, 133*(6), 649-667. doi.org/10.1061/(ASCE)0733-9429(2007)133:6(649)

Vetsch, D. F., Siviglia, A., Bacigaluppi, P., Bürgler, M., Caponi, F., Conde, D., et al. (2020). System Manuals of BASEMENT, Version 3.1. Laboratory of Hydraulics, Glaciology and Hydrology (VAW). ETH Zurich. Available from www.basement.ethz.ch.

Weiss, R., & Bahlburg, H. (2006). A note on the preservation of offshore tsunami deposits. *Journal of Sedimentary Research, 76(*12), 1267-1273. doi.org/10.2110/jsr.2006.110

Wentworth, C. K. (1922). A scale of grade and class terms for clastic sediments. *The journal of geology, 30*(5), 377-392. doi.org/10.1086/622910

Woodruff, J. D., Donnelly, J. P., Mohrig, D., & Geyer, W. R. (2008). Reconstructing relative flooding intensities responsible for hurricane-induced deposits from Laguna Playa Grande, Vieques, Puerto Rico. *Geology, 36*(5), 391-394. doi.org/10.1130/G24731A.1

Yoshikawa, S., Kanamatsu, T., Goto, K., Sakamoto, I., Yagi, M., Fujimaki, M., et al. (2015). Evidence for erosion and deposition by the 2011 Tohoku-oki tsunami on the nearshore shelf of Sendai Bay, Japan. *Geo-Marine Letters, 35*(4), 315-328. doi.org/10.1007/s00367-015-0409-3